

Characterization, surface treatment and nanofabrication by charged particle beams

Antti Peltonen

Characterization, surface treatment and nanofabrication by charged particle beams

Antti Peltonen

A doctoral dissertation completed for the degree of Doctor of Science (Technology) to be defended, with the permission of the Aalto University School of Electrical Engineering, at a public examination held online at the link:
<https://aalto.zoom.us/j/62279161123> and at the lecture hall TU2 of the TUAS building (Otaniementie 17, Espoo, Finland) on the 15th October 2021 at 13:15.

Aalto University
School of Electrical Engineering
Department of Micro- and Nanosciences
Micro and Quantum Systems Group

Supervising professor

Prof. Ilkka Tittonen, Aalto University, Finland

Preliminary examiners

Prof. Krisztián Kordás, University of Oulu, Finland

Dr. Marko Vehkamäki, University of Helsinki, Finland

Opponent

Prof. Nonappa, Tampere University, Finland

Aalto University publication series

DOCTORAL DISSERTATIONS 125/2021

© 2021 Antti Peltonen

ISBN 978-952-64-0510-0 (printed)

ISBN 978-952-64-0511-7 (pdf)

ISSN 1799-4934 (printed)

ISSN 1799-4942 (pdf)

<http://urn.fi/URN:ISBN:978-952-64-0511-7>

Unigrafia Oy

Helsinki 2021

Finland



Author

Antti Peltonen

Name of the doctoral dissertation

Characterization, surface treatment and nanofabrication by charged particle beams

Publisher School of Electrical Engineering**Unit** Department of Micro- and Nanosciences**Series** Aalto University publication series DOCTORAL DISSERTATIONS 125/2021**Field of research** Photonics and nanotechnology**Manuscript submitted** 22 April 2021**Date of the defence** 15 October 2021**Permission for public defence granted (date)** 22 June 2021**Language** English☐ **Monograph**☒ **Article dissertation**☐ **Essay dissertation****Abstract**

Surface characterization and modification methods are an essential part of modern micro- and nanofabrication. Over the course of nine decades, electron microscopy has emerged as the main analysis method for a wide variety of materials. Developed in parallel with machines utilizing beams of electrons, focused ion beam systems have made their way from early analysis tools to include options for sophisticated fabrication of miniaturized devices. With a combined method of implementing electron and ion beams into the same machine, the number of analysis options has increased.

In this thesis, three charged particle-beam methods are introduced that play a pivotal role throughout the work. While electron microscopy, electron tomography and focused ion beam are all established methods, in this work they are applied in materials analysis. In addition, in this work a focused ion beam is used as the main fabrication method in realizing both microdevices and thin-film device platforms. Several other standard fabrication techniques are applied in various processes throughout the work in realizing the presented applications.

Focused ion-beam milling is applied to produce a device platform for low temperature physics applications. Focused ion-beam method also allows a rapid nanofabrication of silicon structures by gallium mask doping of silicon. Functional devices are fabricated by a combination of focused ion-beam doping and dry etching. This hybrid fabrication method enables high aspect ratio micro- and nanostructures. Charged particle beam based material characterization methods are applied to compound Nafion thin films for electroanalytical filtering applications. A standard negative staining method using uranyl formate was applied to Nafion thin films and is shown to improve both contrast and resolution in electron tomography. A new sample preparation method is developed and deployed together with new imaging modes enabling imaging of beam-sensitive Nafion in high resolution. A finger prick blood test strip based on the filtering properties of Nafion and carbon nanotubes is developed. The electrodeposition of copper on carbon nanotube fiber bundles is shown to be capable of increasing the electrical conductance of the bundle, and the copper growth mechanism of bundles is explained. Also it is shown that the corrosion protection of chromium nitride on steel is increased by closing the surface pinholes with an atomic-layer-deposited nanolaminates. Moreover a fabrication method of dual-type nanowires on a single substrate is introduced. Dual-type nanowires are fabricated in a novel method, that enables the fine tuning of the chemistry and optical properties of the nanowires for optical sensor applications.

Keywords Focused ion beam, electron tomography, nanofabrication, dry etching, atomic layer deposition, FIB**ISBN (printed)** 978-952-64-0510-0**ISBN (pdf)** 978-952-64-0511-7**ISSN (printed)** 1799-4934**ISSN (pdf)** 1799-4942**Location of publisher** Helsinki**Location of printing** Helsinki **Year** 2021**Pages** 144**urn** <http://urn.fi/URN:ISBN:978-952-64-0511-7>

Tekijä

Antti Peltonen

Väitöskirjan nimi

Karakterisointi, pintakäsittely ja nanovalmistus varattuja hiukkassuihkuja käyttäen

Julkaisija Sähkötekniikan korkeakoulu

Yksikkö Mikro- ja nanotekniikan laitos

Sarja Aalto University publication series DOCTORAL DISSERTATIONS 125/2021

Tutkimusala Fotonikka ja nanotekniikka

Käsikirjoituksen pvm 22.04.2021

Väitöspäivä 15.10.2021

Väittelyluvan myöntämispäivä 22.06.2021

Kieli Englanti

☐ **Monografia**

☒ **Artikkeliväitöskirja**

☐ **Esseeväitöskirja**

Tiivistelmä

Elektronimikroskoopit ovat vakiinnuttaneet asemansa ensisijaisena analysointimenetelmänä useille eri materiaaleille ja sovelluksille. Elektronisuihkuja hyödyntävien laitteiden rinnalle on vuosien saatossa kehitetty kohdennettuja ionisuihkuja hyödyntäviä järjestelmiä, joiden käyttö on laajentunut materiaalien analysoinnista hienostuneisiin mikro- ja nanovalmistusmenetelmiin. Yhdistämällä kohdennettu elektroni- ja ionisuihku samaan laitteeseen, on analysointi ja mikrovalmistusmenetelmiä saatu monipuolistettua.

Tässä väitöskirjassa esitellään varattuihin hiukkassäteisiin perustuvia menetelmiä, joista kolmea käsitellään tarkemmin. Elektronimikroskopia, elektronitomografia ja kohdennetut ionisuihkut ovat vakiintuneita menetelmiä ja tässä työssä niitä hyödynnetään materiaalien analysointiin. Lisäksi, väitöskirjassa kohdennettuja ionisäteitä käytetään toteutettaessa mikrokokoisia laitteita.

Tässä väitöskirjassa kohdennettua ionisuihkuja käytetään pääasiallisena valmistusmenetelmänä toteutettaessa laitealustaa mikrolaitteille. Samaisella ionisuihkumenetelmällä voidaan seostaa materiaaleja galliumilla hyvin tarkasti, joka mahdollistaa pihin perustuvien korkean aspektisuhteen mikro- ja nanorakenteiden nopean valmistamisen. Toiminnalliset laitteet on valmistettu piille prosessilla, jossa on yhdistetty kuviointi kohdennetulla ionisäteellä ja syvä reaktiivinen ionisyytyys. Uranyyliformaattivärjäysmenetelmän osoitetaan parantavan kontrastia ja erottelukykyä Nafionohutkalvolle tehdyssä elektronitomografiassa. Väitöstyössä kehitetty näytteenvalmistus- ja kuvantamismenetelmä mahdollistaa herkkien Nafionkalvojen kuvantamisen suurella erottelukyvällä. Tässä väitöstyössä esitellyt analysointimenetelmiä hyödynnetään mm. analysoimalla ohuita Nafionyhdistelmäkalvoja, joita käytetään elektroanalyttisissä suodatinsovelluksissa. Työssä esitellään sormenpistoksesta otettavan verinäytteen perustuva testiliuska, jossa hyödynnetään Nafionhiilinanoputkikalvon suodatusominaisuuksia. Työssä esitellään myös kuparin kasvumekanismi sähkösaostusprosessissa hiilinanoputkikuiduille. Hiilinanoputki-kuparikuitujen sähkönjohtavuuden osoitetaan kasvavan esitellyllä menetelmällä. Myös teräksen korroosiosuojausta tutkittiin. Krominitridillä pinnoitettujen teräspintojen korroosionkestävyys paranee merkittävästi, kun pintakerroksessa olevat huokokset kasvatetaan umpeen atomikerroskasvatusmenetelmällä tehdyllä nanolaminaatilla. Lisäksi väitöstyössä esitellään valmistusmenetelmä tuplalankarakenne nanolangoille samalle substraatille. Uusi valmistusmenetelmä mahdollistaa nanolankojen koostumuksen ja optisten ominaisuuksien hienosäädön, jota voidaan hyödyntää optisissa antureissa.

Avainsanat Kohdennettu ionisuihku, elektronitomografia, nanovalmistus, kuivaus, atomikerroskasvatus, FIB

ISBN (painettu) 978-952-64-0510-0

ISBN (pdf) 978-952-64-0511-7

ISSN (painettu) 1799-4934

ISSN (pdf) 1799-4942

Julkaisupaikka Helsinki

Painopaikka Helsinki

Vuosi 2021

Sivumäärä 144

urn <http://urn.fi/URN:ISBN:978-952-64-0511-7>

Preface

The research presented in this dissertation has been carried out over the years in collaboration with several research groups and individuals from diverse fields. The experimental work has been accomplished in Micronova, the cleanroom facilities for micro- and nanotechnology research, and in Aalto Nano Microscopy Center (NMC).

I would like to thank a small group of people for their scientific contributions in publications and throughout the different phases of the thesis work. I would like to show my gratitude for the supervising professor Ilkka Tittonen for accepting the challenge. I would like to show my gratitude for professors: Harri Lipsanen, Janne Ruokolainen, Tomi Laurila, Jukka Pekola, Jari Koskinen, Pekka Kuivalainen, Esko Kauppinen, Hung Q. Nguyen and Juha Muhonen. Acknowledgements and gratitude to researches and co-authors of publications: Jani Seitsonen, Nikolai Chekurov, Victor Ovchinnikov, Jarkko Etula, Niklas Wester, Elli Leppänen, Vladislav Khayrudinov, Lauri Sainiemi, Joona-Pekko Kakko, Hua Jiang, Camilla Tossi, Andrey Shchepetov, Veer Dhaka, Kestutis Grigoras, Pyry-Mikko Hannula, Jari Aromaa, Jarmo Leppäniemi and Perttu Sippola.

Acknowledgements for prof. Krisztián Kordás and Dr. Marko Vehkamäki for their meticulous, but unrewarded efforts for pre-examining the thesis. And I would like to give credit for professor Nonappa, for graciously accepting the duty of an opponent.

Special acknowledgement goes to co-author, colleague, a complete expert in electron tomography and adjunct professor in molecular genetics Peter Engelhardt for scientific rigor, guidance in various ways and numerous late night discussions of various topics including microscopy, sample preparation, biology, longevity, leadership, funding, new discoveries, particle physics and cosmology.

Espoo, September 11, 2021,

Antti Peltonen

Contents

Preface	i
List of Publication	v
Author's Contribution	vii
List of Abbreviations	ix
1. Introduction	1
2. Operating Principles of Electron and Ion Beams.....	5
2.1 Electron Microscopes	5
2.1.1 Charging In Electron Microscopy.....	6
2.2 Electron Tomography	8
2.3 Focused Ion-Beam Systems.....	12
2.3.1 Milling Side Profiles.....	16
3. Basic Microfabrication Methods	18
3.1 Electron Beam Lithography.....	18
3.2 Chemical Vapor Deposition.....	19
3.3 Physical Vapor Deposition	20
3.4 Atomic Layer Deposition	20
3.5 Metallorganic Vapour Phase Epitaxy	22
3.6 Vapour-Liquid-Solid Mechanism.....	23
3.7 Reactive Ion Etching	24
4. Results and Discussion	26

4.1	Silicon Nitride Membrane Device Platform Fabrication	26
4.1.1	Charge Cancelling	28
4.1.2	Stress Cancelling	29
4.2	Device Fabrication By FIB Surface Doping	30
4.3	Nafion Film Characterization For Bio Sensor Applications ...	32
4.4	Surface Passivation By ALD Nanolaminates	40
4.5	Copper Electrodeposition On Carbon Nanotube Fibers.....	43
4.6	Surface Treatment For Growing Nanowires	45
5.	Summary And Outlook.....	49
References		53
Publication I		61
Publication II		73
Publication III		85
Publication IV		97
Publication V		107
Publication VI		115
Publication VII		123
Publication VIII		131

List of Publications

This thesis consists of an overview and of the following publications which are referred to in the text by their Roman numerals.

- I** A. Peltonen, J. Etula, J. Seitsonen, P. Engelhardt, and T. Laurila, Three dimensional fine structure of nanometer scale Nafion thin films, *ACS Adv. Polym. Mat.*, 3, 2, 1078-1086, 2021.
- II** E. Leppänen, A. Peltonen, J. Seitsonen, J. Koskinen, and T. Laurila, Effects of Thickness and additional elements on the filtering properties of a thin Nafion layer, *J. Elec. Chem.*, 843, 12-21, 2019.
- III** J. Leppäniemi, P. Sippola, A. Peltonen, J. J. Aromaa, H. Lipsanen, and J. Koskinen, Effect of surface wear on corrosion protection of steel by CrN coatings sealed with atomic layer deposition, *ACS Omega*, 3, 1791-1800, 2018.
- IV** A. Peltonen, H. Nguyen, J. Muhonen, and J. Pekola, Milling a silicon nitride membrane by focused ion beam, *J. Vac. Sci. Technol. B*, 34, 2016.
- V** P-M. Hannula, A. Peltonen, J. Aromaa, D. Janas, M. Lundström, B. P. Wilson, K. Koziol, and O. Forsen, Carbon nanotube-copper composites by electro-deposition on carbon nanotube fibers, *Carbon*, 107, 281-287, 2016.
- VI** J-P. Kakko, T. Haggren, V. Dhaka, T. Huhtio, A. Peltonen, H. Jiang, E. Kauppinen, and H. Lipsanen, Fabrication of dual-type nanowire arrays on a single substrate, *Nano Lett.*, 15, 3, 1679-1683, 2015.
- VII** N. Chekurov, K. Grigoras, L. Sainiemi, A. Peltonen, I. Tittonen, and S. Franssila, Dry fabrication of microdevices by the combination of focused ion beam and cryogenic deep reactive ion etching, *J. Micromech. Microeng.*, 20, 2010.
- VIII** N. Wester, B. Mikladal, I. Varjos, A. Peltonen, E. Kalso, T. Lilius, T. Laurila, and J. Koskinen, Disposable Nafion-coated single-walled carbon nanotube test strip for electrochemical quantitative determination of acetaminophen in finger-prick whole blood sample, *Anal. Chem.*, 92, 19, 13017-13024, 2020.

Author's Contribution

Publication I:

The author had a major role in this publication. He diluted and spin-coated all Nafion samples. He stained and prepared all samples. He conducted STEM tomography tilt series recordings and reconstructions. He conducted reconstruction data interpretations and had a major role in interpretation of all results. The author participated in the literature review, prepared all associated supplementary material and wrote a major part of the article manuscript.

Publication II:

The author prepared the samples for cross-sectioning, conducted the FIB-SEM cross-sections and associated FIB-SEM results interpretation. He participated in the interpretation of TEM results and the writing of the manuscript experimental section.

Publication III:

The author conducted the FIB-SEM cross-sections, participated in the interpretation of the cross-section SEM and EDX results. The author contributed to the writing of the manuscript.

Publication IV:

The author had a major role in this publication. He observed the phenomena, did all sample preparations, planned and implemented the whole experimental part. The author conducted the literature review and wrote the manuscript.

Publication V:

The author conducted the FIB-SEM cross-sections, imaging and EDX measurements. He contributed to the interpretation of SEM, FIB and EDX results. The author also participated in the writing of the manuscript.

Publication VI:

The author participated in preparing the FIB-SEM cross-sections. He also contributed in EDX and STEM imaging and in the analysis of results from these measurements. He also participated in the writing of the experimental part of the manuscript.

Publication VII:

The author contributed to the microbridge modification using the conventional FIB-milling method. The author participated in the manuscript writing.

Publication VIII:

The author contributed to the sample preparation for FIB-SEM and conducted the FIB-SEM cross-sections. He participated in the interpretation of SEM results and in writing of the FIB-SEM parts of the manuscript.

List of Abbreviations

1D	One dimensional
2D	Two dimensional
3D	Three dimensional
AA	Ascorbic acid
BOX	Buried oxide
CCP	Capacitively coupled plasma
CNT	Carbon nanotube
CoTE	Coefficient of thermal expansion
CryoET	Electron cryotomography
CV	Cyclic voltammetry
CVD	Chemical vapor deposition
DF	Dark field
DND	Detonation nanodiamond
DOF	Depth of focus
DPV	Differential pulse voltammetry
DRIE	Deep reactive ion etching
EBID	Electron beam induced deposition
EBL	Electron beam lithography
EBW	Electron beam writer
EDS	Energy dispersive spectroscopy, same as EDX
EDX	Energy dispersive X-ray spectroscopy
EM	Electron microscopy
EMT	Electron microscope tomography

List of Abbreviations

FEG	Field emission gun
FIB	Focused ion-beam system
FIB-SEM	Dual-beam focused ion-beam instrument equipped with SEM
FIBSIMS	Focused ion-beam secondary ion mass spectrometry
FWHM	Full width at half maximum
GaAs	Gallium arsenide
GAE	Gas assisted etching
GFIS	Gas field ion source
GIS	Gas injection system
HAR	High aspect ratio
HIM	Helium ion microscope
HR	High resolution
HSS	High-speed steel
IBID	Ion beam induced deposition
InP	Indium phosphide
LM	Light microscopy
LMAIS	Liquid metal alloy ion source
LMIS	Liquid metal ion source
LSV	Linear sweep voltammetry
MEM	Maximum entropy method
MEMS	Microelectromechanical systems
MOVPE	Metallorganic vapor phase epitaxy
NEMS	Nanoelectromechanical systems
NP	Nanoparticle
NW	Nanowire
PBS	Phosphate-buffered saline
PEC	Proximity effect correction
PECVD	Plasma-enhanced chemical vapor deposition

PR	Photoresist
PTFE	Poly(tetrafluoroethylene)
PVD	Physical vapor deposition
RDE	Rotating disk electrode
RF	Radio frequency
RI	Refractive index
RIE	Reactive ion etching
RT	Room temperature
RTS	Residual tensile stress
SAE	Selective-area epitaxy
SE	Secondary electron
SEM	Scanning electron microscope
SIMS	Secondary ion mass spectrometer
SiN _x	Silicon nitride
SiO ₂	Silicon oxide
STEM	Scanning transmission electron microscopy
STM	Scanning tunneling microscope
SWCNT	Single-walled carbon nanotube
ta-C	Tetrahedral amorphous carbon
TBA	Tertiarybutylarsine
TBP	Tertiarybutylphosphine
TEM	Transmission electron microscope
UA	Uric acid
VLS	Vapor-liquid-solid
VLSI	Very large scale integration
WDS	Wavelength-dispersive X-ray spectroscopy
XTEM	Cross-sectional transmission electron microscopy

1. Introduction

Où est-ce que vous allez, votre majesté de Broglie?

In 1929 Prince Louis de Broglie won a Nobel Prize for his 1924 postulation of the wave nature of electrons and a suggestion of the wave nature of matter. His description of electron wavelength

$$\lambda = h/(m_e v)$$

together with the formula for electron potential

$$eV = \frac{1}{2} m_e v^2$$

gives a theoretical resolution of 3.88 pm for 100 kV electrons. The simplest atomic hydrogen has a diameter of 1 Å (100 pm), thus high energy electrons provide us with resolving power that is far below the atomic resolution. Beams of electrons are used, firstly, to image details that are below the Abbe (1840-1905) diffraction limits of light microscopy (LM), secondly, to excite atomic electrons for elemental analysis in production of x-rays, welding and, thirdly, for high resolution (HR) exposures in micro- and nanoelectromechanical systems (MEMS/NEMS). Even though LM has not lost its usability and area keeps improving^{1,2}, there is a strong need for ever more powerful electron microscopes³. Beams of focused ions have been used for the same purposes as electron beams, but in addition also for milling and doping. When electron and ion beams are combined in one single tool, these two technologies enable more capabilities than they would when the tools are built separately.

Electron microscopes have been around for almost 100 years. In 1926 the first electromagnetic lens was invented by Hans Busch. This was followed a few years later when, in 1932, Ernst Ruska and Max Knoll built the first ever transmission electron microscope (TEM). This was soon followed by a scanning electron microscope (SEM) some ten years later and a scanning transmission electron microscope (STEM) by Manfred von Ardenne in 1938⁴. The STEM was further developed by Albert Crewe in 1963⁵ who was a keen biologist, and a year later in 1964 came up with a field emission gun (FEG) that established new records in electron microscopy (EM) resolution. Ruska won the 1986 Nobel prize for inventing the transmission electron microscope jointly with Gerd Pinning and Heinrich Rohrer for their scanning tunneling micro-

scope (STM). The new technology of electron microscopy enabled researchers for the first time to detect features of the size of viruses, and the images of the tobacco mosaic viruses won the honor of being the first ever images of viruses in 1939⁶. Unfortunately, the images during the first decades of electron microscopy were blurry and it took 60 years for the first correction system to emerge. Once thought impossible, it took one experimental physicist, Maximilian Haider, to devise a correction for the electron-optical aberration of magnetic lenses in 1997. The world's first correction system for EM to reveal an atomic resolution was achieved. Since then, microscopes have increased steadily in size and resolving power. Applications in biology and medicine were the driving force for the development of electron microscopy, but today there is nearly no industry or physical science that would not benefit directly or indirectly from electron microscopes. Instruments based on beams of electrons are used in characterization, material science, advanced manufacturing, research, metrology and process control.

The first attempt to generate a microscope based on ions was in 1975 by Orloff et al.⁷ for the H^+/H_2^+ beam. This was soon followed by G. Roy Ringo and V. E. Krohn⁸ who developed a 100 nm spot size beam from a gallium source. In the 1980's a tool with a 10 nm beam was introduced, and that was immediately adopted by the semiconductor industry. The driving force for the development of early focused ion-beam (FIB) systems was for the testing of physical failures, circuit modification and repairs needed in the semiconductor industry. Later, the general interest in using FIB has shifted more towards fabrication of nanostructures, new applications in biology and the whole spectrum of material sciences.

The long history of these tools shows that they are not going to wither and vanish away. In contrast, their importance is expected to increase. Analysis and characterization methods play a critical role in nearly every area of modern natural science or industrial research, and the need for ever more powerful microscopes has resulted in a wide industry and vast product range based on charged particle beams. Electron and ion-beam instruments have been developed in parallel as separate systems, and nowadays more commonly as dual-beam or even triple-beam systems. The combination of different techniques in a single system has made it possible to improve the beam control and to realize variety of new applications such as photonic, and micro-fluidic devices, sample preparation for high quality TEM, and secondary ion mass spectrometry (SIMS) analyses, 3D reconstructions by the slice-and-view recording approach and maskless implantation. The FIB is one of the few tools available for producing complex 3D HR structures and to perform tomography on any solid material.

The development of these systems still continues towards new application fields. This thesis focuses on finding new uses for charged particle beams, surface treatment and surface characterization. This thesis aims to push forward the level of understanding of the versatility of these tools when defining patterns by drawing and exposure, characterizing materials at high resolution and modification of existing structures.

In Publication I and Publication IV, the serious detrimental issues arising from the use of charged particle beams are presented. In Publication IV, the positively charged ion beam on insulating silicon nitride (SiN_x) thin film causes the film to buckle that results in a catastrophic breaking of the entire film. The introduction of charge-conducting copper wire patterns on the film is shown to reduce the charging sufficiently to a degree at which nitride film perforation by ion milling becomes possible. This method becomes especially useful, when the film perforation is the last process step and traditional lithography and etching methods cannot be applied.

In Publication I, Nafion thin films are imaged with STEM in order to reveal their fine morphology. In order to predict and design electrochemical and filtering properties of Nafion thin films, it is necessary to be able to characterize the morphology of the film. Nafion is known to have the structure of a dense Teflon backbone which is permeated by undulating hydrophilic channels. The precise morphology of these channels has not been known, but in Publication I the fine details of these channels are shown for the first time by uranyl formate (UF) staining and STEM tomography. Previously, it has proven to be difficult to image Nafion with electron microscopy in high detail due to its fragility and beam-sensitive nature. Polymer materials are known to be heavily charging under charged particle bombardment and, in addition, Nafion is very beam sensitive, meaning that the irradiation easily deforms the material. To stabilize the electron beam induced charging on an insulating Nafion surface, we deposit a thin layer of carbon on the top of the film. Once the film is stabilized, a tilt series is recorded and reconstruction of the three-dimensional (3D) morphology of the film is revealed.

Further Nafion film structure studies are performed in Publication II, where detonation nanodiamonds (DNDs) are introduced into the polymer to form composite films. The filtering properties of these films are characterized by electrochemical and structural studies. To reveal the film structure of Nafion DND films, TEM imaging and FIB cross-sections are reported in Publication II.

The channels composed of anionic sulphonate groups induce the filtering properties of Nafion by letting through cations and by blocking anions. Publication VIII discusses the elimination of interfering anionic signals from human plasma by a Nafion carbon nanotube (CNT) coating on electrodes. The combination of a high signal-to-noise ratio in the electrochemical detection of CNTs and the unusual filtering properties of Nafion, the two are used on top of each other in disposable finger-prick blood sample test strips. In clinical settings, overdosed drugs are identified with spectrophotometry, which is carried out in specialized laboratories and it is a semi-rapid method. The finger-prick test strip introduced in Publication VIII is low cost and able to reliably detect trace amounts of drugs in blood serum samples without additional steps. The introduced process is an industrially-scalable dry transfer process and can be applied on a wide range of substrates.

Carbon nanotubes and fibers made of bundles of nanotubes have a wide range of interesting properties. In addition to the electrochemical detection method, CNT fibers have exceptional mechanical properties, as well as high thermal and electrical

conductivity. Publication V presents an electrochemical deposition of copper on carbon nanotube fiber, which increases the specific conductance of the fiber by a factor of 9. The growth mechanism and results are examined with FIB cross-sections, and electron-beam-induced energy dispersive elemental analysis.

The effects of corrosion prevention on a steel surface by thin atomic-layer surface coatings are studied in Publication III. After the wear tests on steel samples, the FIB milling cross-sections of the surface are analyzed, followed by a careful x-ray elemental analysis to determine the effect of surface wear.

Attention is given to how some negative side effects of scanning the sample surface with charged particle beams can be turned to our advantage. Doping the surface with gallium is usually considered as an adverse effect due to changing the material properties. In Publication VII, this doping effect is utilized to realize rapid prototyping of 3D silicon structures by combining maskless gallium implantation and dry etching. In Publication VI, electron beams are used to pattern the array of two types of nanowires on the surface of a single gallium arsenide substrate. In addition, electron-beam-induced elemental analysis is used to characterize the FIB-SEM cross-sections of the sample.

2. Operating Principles of Electron and Ion Beams

Modern measurement tools relying on scanned particle beams have become easy to operate. This has reduced the apparent skill requirements of the operator, and has resulted in some operators not taking sample preparation and image acquisition seriously⁹. In EM measurements, everything is not necessarily correct or reliable, or cannot be intuitively deduced. This chapter introduces the three main charged particle beam methods used in this work and gives some examples of sample treatment considerations related to these methods.

2.1 Electron microscopes

In an electron microscope, accelerated electrons are hurtled in a vacuum towards the object, and with the aid of electromagnetic fields the beam of electrons is focused on the sample surface. When hitting the surface, various signals from the surface are captured by a detector and processed to form an image on a microscope display. The electron micrographs do not show colors, as the grey-scale images taken only show the electron waves and not those of light. In SEM, the contrast in the micrograph is mainly created by the topography of the sample, atomic mass of the elements, and the tilt angle of the incident beam, whereas in TEM the image shows the electron densities projected through a thin (~100 nm thick) sample. The incident electron beam knocks out secondary electrons (SE) from the sample in an inelastic interaction, and is fairly weak and largely originates from a thin surface layer some 10 nm deep. The SE signal yield is increased significantly by increasing glancing angles exhibiting clear topography contrast¹⁰, but is not good at elemental analysis as the secondary electrons are not associated with any particular surface atom but are shared between them. Different signals carry different information of the sample, and therefore several different types of detectors are needed. If the energy of the incident electrons is high enough they may penetrate deep into the sample, and can even travel through the thinner samples. If enough electrons can pass through the sample, transmission electron microscopy becomes possible.

Heat, particles and radiation are created in inelastic interactions with the sample. In elastic scattering of electrons no kinetic energy is released. Electron bombardment also causes the cross-linking of volatile organic compounds (VOC) present in air, leading to continuous growth of contamination on the sample surface¹¹. Unless the VOCs are removed by e.g. oxygen plasma, they can cause extra features on micrographs.

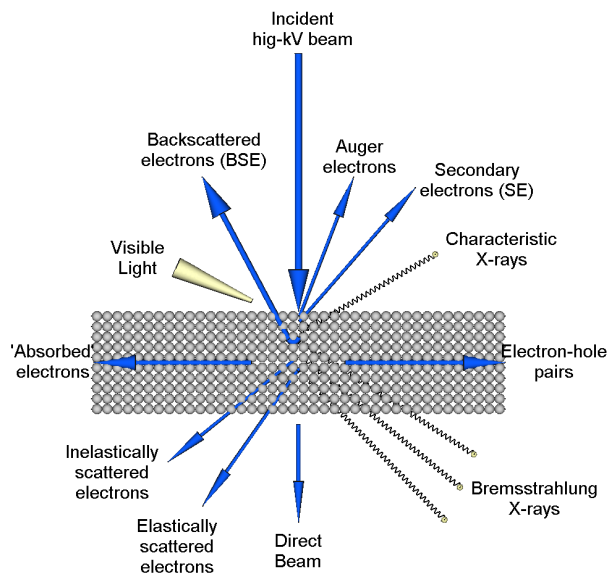


Figure 1. Interactions of an electron beam with a specimen. Various mechanisms between the incident beam and matter induce different particles of various energies to be emitted from different depths. Some electrons may even travel through a thin sample without noticeable interaction.

2.1.1 Charging In Electron Microscopy

Charge build-up in operating scanning electron beams has been known since the invention of the first television sets^{12,13}, the first SEMs as early as 1939¹⁴ and when operating with insulating EM samples¹⁵. As charging effects play a major role in EM and FIB-SEM processes, it is essential to minimize the detrimental effects¹⁶ and enhance the beneficial ones. Charge build-up effectively disturbs the imaging process, interferes in milling with FIB and may destroy sensitive samples.

Charging of the sample in EM is meant to describe the build-up of, either positive or negative potential, near or at the sample surface, while it is being irradiated by a particle beam⁹. Any increase in the surface potential alters the landing energy of the incident beam, as the beam is pushed away from the target area. Sample surface charging results in changes in magnification, potential errors⁹ and increases beam drift. The beam that is deflected is not collected by a sensor, resulting in instability of the secondary electron image intensity, image distortion and poor resolution.

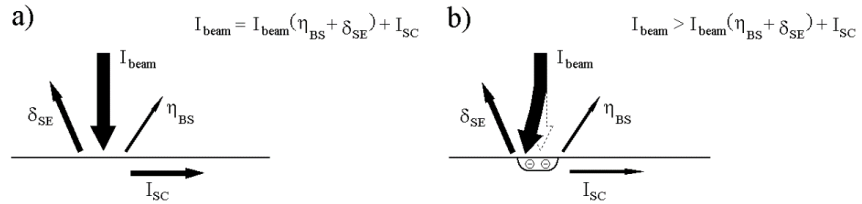


Figure 2. Diagram of sample charging by electron irradiation, where (I_{SC}) is the specimen current flowing to the ground, η is the backscattered electron coefficient and δ is the secondary electron coefficient. (a) In an ideal conductor the charge entering the sample is rapidly removed leading to neutral surface net charge. (b) In a poorly conducting sample, charge disequilibrium is reached rapidly, which results in charging, beam deflection and to poor measurement results.

The mechanism of charging process is complex, and not fully understood¹⁷⁻¹⁹. The goal in charge cancelling is to achieve a status, where the incoming, and outgoing charges are equal. The most common methods to overcome charging of EM samples are conductive layer deposition²⁰, careful grounding of the sample and utilization of a low energy electron flood gun for neutralization. An EM operator should take good care of alleviating the charging by ensuring that the sample is not just partly grounded and that the charging behavior in one sample may vary between different tools. For systems that are not equipped with a flood gun, the SEM electron beam can be used instead. In this case the defocused electron current (which is three times larger) must be applied in comparison to the used ion current, however most available systems are equipped with a built-in automatic “neutralize” function. In less insulating samples, lower beam currents can be used to give charged particles more time to be conducted away from the target area.

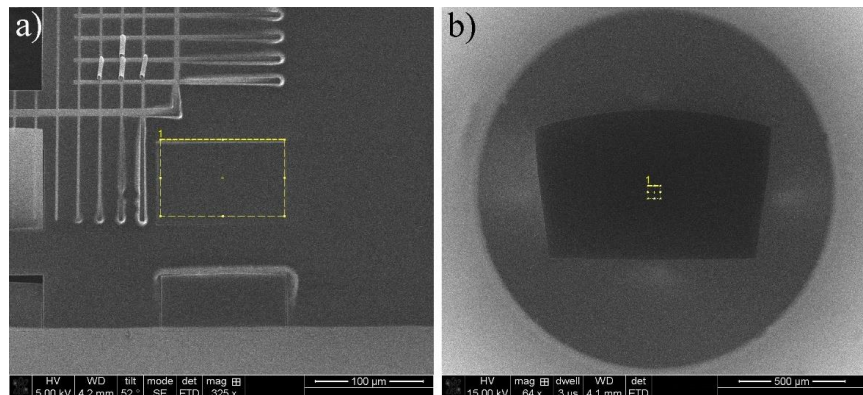


Figure 3. Charging caused by an ion beam. Yellow square indicates the ion milling pattern. (a) A glowing discharge build-up on the copper wires on a silicon nitride membrane after ion beam milling. The edge of the milled area below the yellow square is also glowing. (b) Heavy charging after ion beam irradiation, causing huge distortions in imaging of a square silicon nitride window.

Depending on the particular application, charging of the surface of the sample might be beneficial or detrimental. In a typical SEM, the electron source is pointing down-

wards towards the sample, which is facing up. If the insulating sample has been charged heavily enough with electrons, it is possible that enough electrons are being emitted from the charged area forming an incident electron source. Enough electrons are emitted, to allow the forming of a detailed SE image for inspecting the chamber and pole piece (Figure 4b). The presented method shows the power of specimen charging.

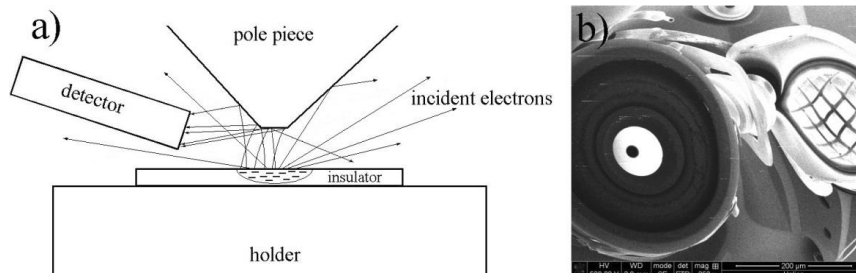


Figure 4. “EM selfie” of an SEM chamber. a) Piece of an insulator is used as the primary electron source, after charging it with SEM. Secondary electrons are captured by the detector and the imaging of the chamber components is formed. This is a very convenient method for quickly detecting contamination in the pole piece aperture. b) Resulting SE image of the tip of the pole piece utilizing a heavily charged insulator as an electron source.

2.2 Electron Tomography

Electron microscope tomography (EMT) is a less known technique within the scientific community in spite of the fact that 3D reconstructions from electron micrographs were put forward already in 1968²¹⁻²³. Tomography means acquisition and visualization of a 2D slice series to generate a 3D reconstructed image (a tomogram) of the original sample. In EMT, the electron beam transluents the target from one direction into one plane, where the structures of the specimen are superimposed due to the orthographic nature of EM. These “flatworld” 2D TEM micrographs carry less information about the system as the depth information has been superimposed into this one projection. To overcome distortions in this representation, all dimensional information must be recorded and presented in a way that is most appropriate. Ignoring one dimension completely may lead to severe interpretation errors as many of the internal structures of the sample that seem attached, are in reality separated. Therefore, in situations where the 3D structures of the specimen matter, preventing the loss of meaningful information in representations must be considered.

The EMT aims at storing the complete structural information of the sample at the selected magnification. The sample is imaged from multiple angles. In theory, the most accurate result without any information loss is achieved when the images are recorded from all possible sides of the sample, meaning all angles between +90° and -90° with respect to the normal of the surface. This rule is depicted in Figure 5a as the surface of the transparent semisphere around the specimen. In practice, acquiring such a perfect tilt series is limited by time and sample irradiation durability, not to

mention limitations in the recording and reconstruction hardware. The simplest way to acquire the depth information is to take a stereopair, that is two images taken from different angles. The stereopair will result in a static image that has a better resolution than a single image, but this method is not applicable to reconstructions due to static limitations. In EMT, the established methods are to collect the tilt series by TEM or STEM using one or two tilt axis and capturing an image at certain increments. Unfortunately, unrecorded tilt angles add up to information loss in the recording, which leads to distortions and noise in the final reconstructions. The more information that is lost by skipping the tilt angles, the more prominent the distortions becomes in the final reconstructions. The advantage of the STEM mode of the recorder over the TEM mode is its dynamic focusing condition, that keeps the focus uniform across the tilted specimen. This allows fully focused images for the tilt series, that are sharper than in TEM mode recordings. The second advantage of the STEM mode is that, as a narrow but bright electron probe is used for scanning, the beam penetrates thicker samples better than TEM⁵. Historically, the fear of causing irradiation damage to the samples in STEM mode caused delays in adopting the method. In practice, a more energetic beam, higher kV, must be used in TEM mode to achieve a corresponding image quality, but with a cost of more irradiation-induced damage.

The axial tilt approach is different from the FIB-tomography or microtome serial sectioning. An FIB-SEM tomography series can be performed for a wide variety of materials²⁴, and is often referred to as a slice-and-view approach. In the slice-and-view method, the sample is milled by the ion beam (one thin slice at a time) and a series of images is recorded from the so-called block faces that are uncovered by the ion beam milling. Microtome sectioning works in a similar way, in which a block of material is sliced into thin slices. The difference between microtome sectioning and FIB-tomography is that the microtome slices can be stored for later examination. Microtome sectioning is limited by the blunting of the blade and can cut materials up to the hardness of aluminum. Both methods tend to be destructive to the sample, as the sample is either cut into thin slices, or is evaporated. Both slice-and-view and microtome sectioning methods are more suitable for larger sized samples^{25,26}. At smaller size samples (e.g. cells, chromosomes, viruses, and large molecules), tomography with transmission electron microscopy is recommended. In order to avoid information loss in the slice-and-view method, the slices should be infinitely thin to record all structural information. In practice, however, this is not possible, as the slices always must have some thickness. A specialized application of electron tomography is electron cryotomography (CryoET), typically used for vitrified biological samples in order to preserve the aqueous structures undistorted for the imaging. Both tomography methods aim at recording 2D images for creating a 3D reconstruction. Both methods suffer from missing information, but not to the extent that would prevent a formation of a meaningful reconstruction.

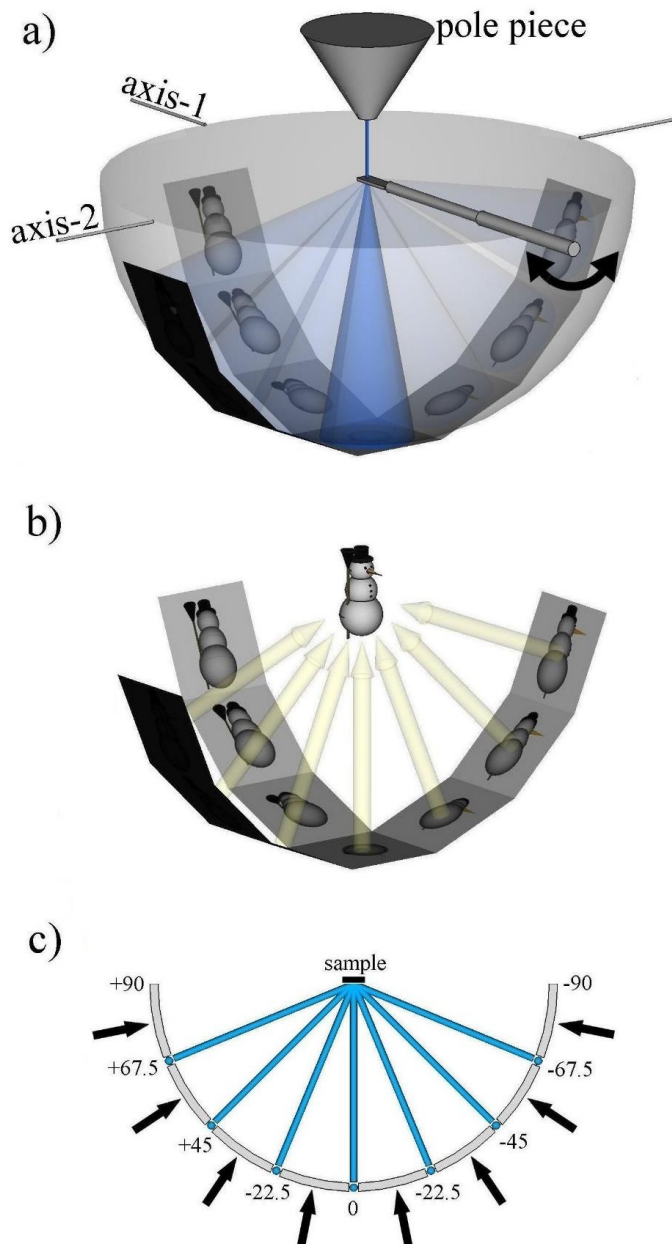


Figure 5. A not-to-scale schematics of electron tomography with a two-tilt axis. a) Tilt series recording by an electron beam (blue beam). The transparent semisphere represents the surface that theoretically provides the complete structural information of the sample. The sample is located on the TEM grid at the center directly under the electron beam. The electron source is fixed, but the rod holding the sample is rotated. In the tool JEOL JEM-2800 used in this work, the distance between the pole piece and the grid is less than 3 mm, which prevents using high tilt angles for the whole TEM grid. b) Radon back-projection. A 3D reconstruction step from recorded images. c) Cross-section of one axis 67.5° to -67.5° tilt range. Electron beam (blue line) records images (blue dots) with 22.5° increments. The grey arches point to the missing data.

In order to collect tomography raw data, the used tool must be equipped with a stage or holder capable of providing large tilt angles at eucentric heights. From various tools and methods available, the success depends on the selection of the most suitable approach. EM tomography is a tedious process, and skills are required to operate an EMT process, however the rewards can be significant.

The sample is transferred on a TEM grid, which is mounted on a special holder, or a rod (Figure 6). The rod is inserted into the vacuum chamber of the electron microscope, and the tilt series is collected either automatically or manually. The goniometer takes care of tilting the sample holding rod. During recording of the tilt series, the sample gets exposed to radiation every time an image is recorded, and extensive radiation damage corrupts any recording attempts. In a standard tilt series an image is recorded every two degrees in the tilt range 72° to -72° (occasionally 60° to -60° is used) resulting in 73 images recorded for raw data. It is up to the skills of an operator to treat the sample and optimize the imaging conditions so that a complete tilt series can be recorded without deforming the specimen.

After recording the tilt series, the micrographs must be aligned. This can be done manually using fiducial markers, or automatically using commercially available software. The projected and aligned images are transformed into 3D reconstruction by Radon back-projection transform, named after the Austrian mathematician Johann Karl August Radon (1887-1956), who invented this mathematical method^{27,28}. The Radon back-projection method has since been further developed, and a custom-made Maximum Entropy Method (MEM)²⁹ was used in this work. The MEM is a criterion how to choose the *correct* variables from an uncertain data set, and in EMT the uncertain data corresponds to the uncertainty in marker locations, inaccuracies in micrographs, etc. The MEM aims at minimizing random errors and noise on the basis of assumptions with regard to shapes and best fit with respect to noise³⁰. It is an iterative procedure and has been used successfully in radio astronomy, infrared spectroscopy and nuclear magnetic resonance imaging.

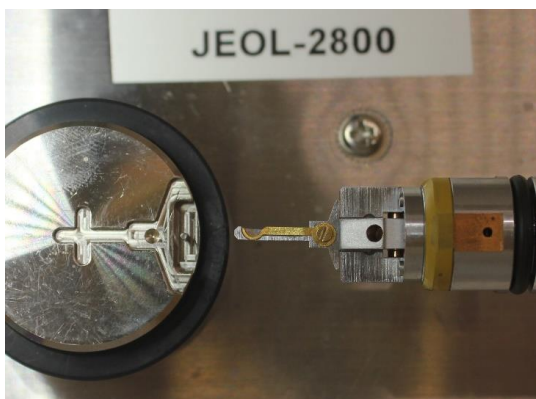


Figure 6. A JEOL JEM-2800 EM high-tilt holder for collecting the tilt series for STEM tomography. A half-cut gold TEM grid is clamped at the holder tip at the center in an image. The gold grids are cut in half in order to make them fit under the pole piece for the high-tilt series in the microscope vacuum chamber. Uncut whole grids could only perform a $\pm 20^\circ$ tilt due to narrow space.

2.3 Focused Ion-Beam Systems

In nanofabrication, the focused ion beam is a well known tool that offers simultaneous HR imaging and flexible micromachining. An FIB system is an optical instrument similar to the SEM, but instead of electron optics and electrons, beams of ions are focused and scanned on the sample by ion optics. The ion column consists of a condenser lens and an objective lens. Electrostatic lenses are used, as the charge/mass ratio of ions in FIB is much lower than that of the electrons in the SEM, electromagnetic components would have to be impractically large³¹. An aperture strip is used to define the beam current and the spot size. The probe size of the beam, that ranges from hundreds of μm 's to nearly 1 nm, determines the volume removal speed and roughness of the milling trace. The possibility of removal and adding of materials in an FIB enables a production of precise 2D and 3D shapes. Equipped with gas injection systems (GISs), a variety of gases can be introduced for local chemical vapor deposition (CVD) or milling enhancers. The material removal feature of the FIB is widely utilized in micromachining, FIB-tomography and in the sample preparation for cross-sectional transmission electron microscopy (XTEM).

In comparison with the SEM, in the FIB, the electron source is replaced with an ion source, that most commonly is based on a liquid metal ion source (LMIS). The LMIS has a long history, and was first reported in 1600 by an English physicist William Gilbert³²⁻³⁵. The first adequate mathematical theory showing that liquids adopt conical shapes under strong electric forces was produced by Taylor, in 1964^{35,36}. In modern liquid metal ion sources used in FIB applications, the liquid metal is heated and wets the surface of a tungsten needle. A strong electric field pulls the metal into a conical shape referred to as a "Taylor cone", with a tip radius in the order of a few nanometers. The electric field between this small tip and the extractor electrode causes ionisation and field emission of the gallium atoms emitting ions, ion clusters, neutrals, microdroplets and light^{35,37}. The ions emitted from this point source can be focused with a modern ion optics down to a few nanometer spot size with full width at half maximum (FWHM) diameter of around 2 nm. The advantage of an LMIS source is that no high vacuum is required. Nearly half of the elements in the periodic table are available as a FIB source as ions^{10,38}, but the vast majority of FIB uses gallium. The low melting temperature of metals make LMIS easy to design, and gallium has a convenient melting point of 30 °C. Even though gallium is chemically reactive, it does not react with a tungsten needle. Other advantages of gallium are its low vapor pressure and wetting properties. These points make a gallium LMIS most stable and long lasting. The very recent interest in liquid metal alloy ion sources (LMAIS)³⁸ provides a promising path for expanding FIB applications even further.

Depth of Focus (DOF) is the distance where the image of the object stays sharp if the object is anywhere within the DOF range. The DOF is mainly dependent on the size of aperture, magnification and working distance. The DOF can be increased by increasing the working distance, reducing the aperture diameter or by reducing magnification³⁹. The DOF is much larger for the SEM than for LM, but for ion beams the DOF can be an order of magnitude higher than for the SEM⁴⁰. A larger DOF makes it easier to image and focus on high aspect ratio (HAR) and 3D structures. Considering that FIB

applications typically involve highly 3D structures, features such as a large DOF become highly useful.

The other advantage of heavier ions in imaging applications is that they can reveal higher contrast between metal crystals compared to the imaging technique using an electron beam. The effect of higher contrast between copper crystals is evident in Figure 37a.

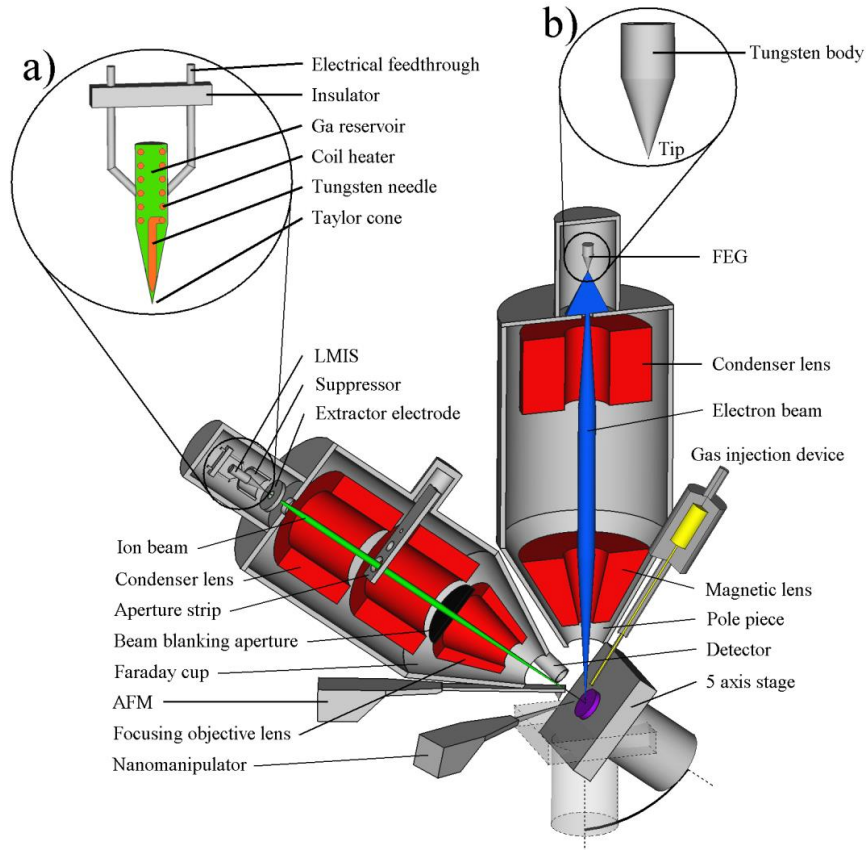


Figure 7. Schematic of a generic FIB-SEM system with most common components. The SEM column stands vertical and the FIB column is at a tilted angle. The detector could be an electron detector or SIMS. The 5-axis stage is depicted at the same tilt angle as the FIB so that the sample (purple disk) surface is perpendicular to the ion beam. a) Gallium is in contact with a tungsten needle and when heated the needle gets wetted. Heated liquid gallium flows to the needle where the opposing forces of surface tension and electric field form the liquid gallium into a Taylor cone³⁷. b) The simple structure of a field emission electron source.

The trend is towards multi beam systems. In addition to the gallium ion beam, the system may have been equipped with electron, argon, or xenon beams⁴¹. The most common dual-beam system is an FIB equipped with an SEM, where the electron beam is used for imaging, energy dispersive spectroscopy (EDX), wavelength dispersive X-ray spectroscopy (WDS) and charge cancelling. Argon and xenon beams can be used in final stage processing to remove the damaged layer after FIB processing and for milling. Both Ar and Xe ions are chemically inert, but only Ar and Ga are reported to contaminate the material surface^{42, 43}. The Xe ion have a larger ion cross-section,

and thus a lower penetration depth compared to Ga, contaminating less the surface. The Xe FIB can speed up large-volume and TEM lamella milling considerably in comparison to a Ga ion beam, while still having a reasonably sharp beam⁴⁴. Both Xe and Ar beams can be added as a third beam into the Ga dual-beam system, forming a triple beam system.

Gas field ion source (GFIS) such as hydrogen and noble gases (e.g. He and Ne) are alternatives to metal sources. The difference between a helium ion microscope⁴⁵ (HIM) and a gallium FIB is that an HIM has relatively low beam current and it lacks a quantitative materials analysis mode (such as EDX). The HIM is less damaging⁴⁴ than the use of a Ga beam and He ions have a higher DOF than Ga beams. The HIM uses a cryogenically-cooled gas field ion source to produce an extremely focused ion probe down to 2.5 \AA ⁴⁶⁻⁴⁹. He ions spread deeper into the target material, due to He having a smaller cross-section. For beams made of lighter mass impacting ions, the impacting energy spreads deeper, and the target atom collision cascade extends less⁴¹ laterally. These effects translate to a smaller sputtering yield^{37,46}, thus making the HIM much slower than the FIB. The lowest currents in the HIM are used for HR imaging, where as the higher currents can be used for the compositional and structural information of the sample⁵⁰. In GFIS technology, the tungsten needle is used for ionization, and the He GFIS can produce narrower beams than the LMIS, and reaches a milling resolution down to 5 nm. An Ne-ion beam can reach a milling resolution of about 20 nm³⁷, approaching the resolution of a Ga ion beam.

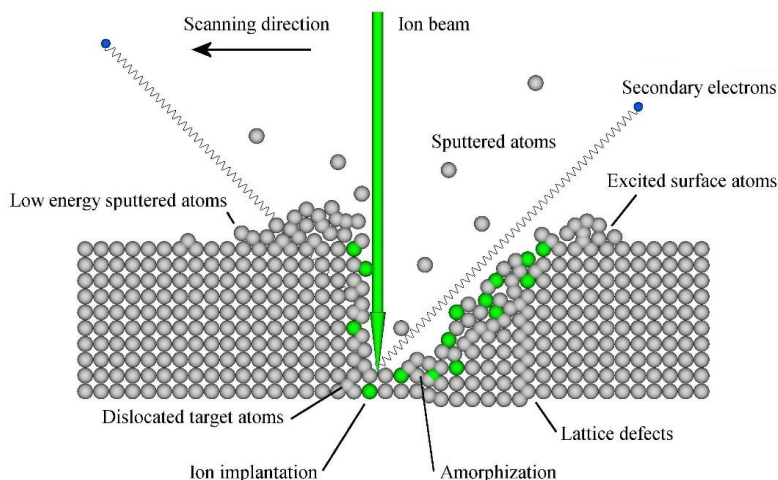


Figure 8. Schematic of FIB milling on a sample surface. When an ion beam hits the sample surface various signals are emitted. Sputtered atoms are in an excited state and are removed to a vacuum or redeposited on the sample. The target surface is permanently modified by the sputtered target atoms, dislocated target atoms, implanted incident ions, amorphization and lattice defects.

When an incident ion beam hits the sample surface it is sputtering the first few monolayers. Below the surface, high energy ions generate plenty of electron-hole pairs, lattice defects and cascade implantation⁵¹. A thin surface layer is amorphized⁵², and is composed of the implanted gallium⁵³ and target atoms. Ion beam irradiation changes

the surface properties of materials permanently⁵⁴, especially those that are electrical, optical or mechanical. The changing of material properties by an ion beam is not an entirely adverse effect, as liquid metal alloy ion sources (LMAISs) are under development aiming to control the tuning of material³⁸. The focused ion beam implantation has also shown to be able to manipulate the stress of metallic thin film structures⁵⁵. Surface charging is increased due to the introduction of a positively charged ion beam, and also secondary electron emission is enhanced by the collisions. Sputtered secondary ions are lost to the chamber vacuum, while others are redeposited on the sample surface as debris around the milling area, or are collected and selected according to their mass by a secondary ion mass spectrometer (SIMS)³⁷. Atoms left on the surface are in an excited state releasing secondary electrons. The sputtering yield can vary a lot depending on the target topography, crystal orientation, beam incidence angle⁵⁶, and beam probe size. Surface topography changes as the milling progresses and also the milling yield increases towards the scanning direction due to the so-called “edge effect”. As the sputtered atoms have increasingly more free space around them, they have a higher probability of escaping the milling location. This useful property can be utilized for faster obstructing material removal for cross-sectional imaging by choosing a line-by-line milling method, which is faster than a regular layer-by-layer milling approach. Milling in confined areas, such as HAR structures, gets increasingly more difficult, as the sputtered atoms efficiently prevent physical sputtering. As the free space around the beam collision point decreases, less sputtered atoms are removed to the vacuum and more incident beam energy is lost to remilling the material that has already been sputtered.

Equipped with a GIS, an FIB-SEM can exploit gas assisted local deposition of the material by CVD, using both electron and ion beams. The CVD can be performed by ion beam induced deposition (IBID)⁵⁷, or using an SEM for electron beam induced deposition (EBID). CVD chemicals (or precursors) are introduced using GIS, and the precursor molecules arrive mostly via surface diffusion, as do the impurities. This has an impact on the quality of the deposited materials as more contaminants and carbon gets trapped into the deposition. The precursor molecules are decomposed due to local heating of the surface caused by the secondary electrons generated by the ion/electron beams. The byproducts are carried away by pumping the chamber while the target molecules end up in local deposition. As the ion beam is capable of producing more secondary electrons than the SEM, the EBID-grown deposits suffer from lower deposition rates. Another drawback of EBID-grown materials are poor electrical properties^{58,59}. IBID offers faster growth rates and better deposit quality, but suffers from the gallium irradiation damage of the substrate, and gallium doping of both the deposit and the substrate. IBID-grown structures are also not so well defined, and they also exhibit deposition halos around the grown structures.

To increase the sputtering yield in HAR structures where milling of more free space is not possible, it is possible to use gas-assisted etching (GAE). GAE for an FIB has been available for four decades⁶⁰⁻⁶² and used extensively for HAR structures and to sharpen etch profiles⁶³. Etching-application-specific etchant gas is decomposed by secondary electrons, and the decomposed products bind chemically to the sputtered atoms

making them more volatile. To enhance the removal of silicon-based residues from the milling area, GIS for Cl_2 , Br_2 , I_2 gases can increase the sputtering yield by 8-fold, whereas XeF_2 can amplify the silicon etching up by a factor of 2800⁶⁴. The gas-assisted sputtering yield is defined as the number of substrate atoms removed by incident ions:

$$Y = \frac{(\text{removed atoms})}{(\text{incident ions})} = \frac{(AR+AS)}{Jt_D},$$

where AR is the number of substrate atoms that have reacted with the gas, AS is the number of substrate atoms removed by physical sputtering, J is the ion flux of the beam, and t_D is the dwell time⁶⁴.

Careful consideration is needed when choosing the correct gas, since some of the gases might be highly aggressive, or spoil the structure by spontaneous isotropic etching⁶⁴. The consequence is that this makes milling faster as the already sputtered residue is not blocking the incident beam from hitting the target atoms.

2.3.1 Milling side profiles

Milling vertical structures with a gallium ion beam leads to side-wall amorphization⁶⁵, implantation and curtaining. The term curtaining is used to express the slight variations in the side wall thickness parallel to the milling direction and can significantly change the interpretation of the revealed structures. Curtaining can be seen clearly in Figures 9, 36 and 37d. The different sputtering rates that inflict the curtaining originates from the phases between the different materials and the sample surface topography. The curtaining becomes more prominent on thicker samples (>20 μm) as the ion beam is focused on the sample surface, but becomes increasingly underfocused deeper in the milling direction, causing increasingly more evident curtaining effect.

Several curtaining mitigation strategies exists, which include sample rocking⁶⁶, embedding in low viscosity resin, tungsten-mask shadowing, excess milling dosing, changing beam parameters, gas-enhanced milling and polishing with finer spot sizes. Sample rocking has become a mainstream method and is carried out by rocking the sample on the stage left and right at a small angle while polishing milling (Figure 9). Even though this method is less accurate and takes more time, it provides a significant improvement to the sample side-wall profile.

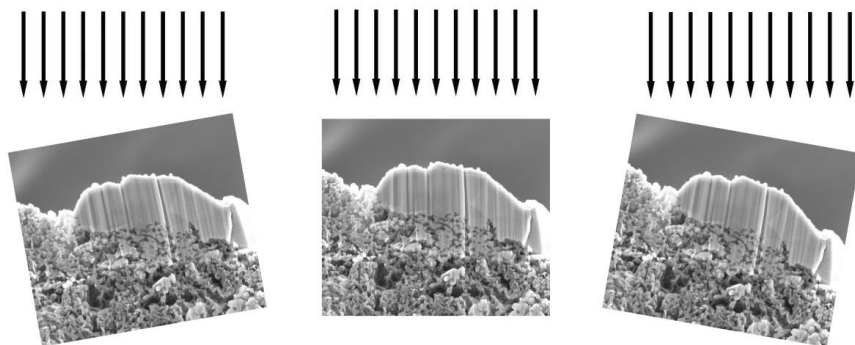


Figure 9. A cross-section of a sample that has suffered from the curtaining effect. Curtaining effect mitigation can be done by surface polishing by rocking the stage from left to right.

3. Basic Microfabrication Methods

Microfabrication consists of different methods that are mostly used in various combinations in order to achieve a desired device, function or structure. Microfabrication is defined by the functional structure being in the range of 0.1-100 μm in size, and the same thickness range is used to define a membrane. Fabrication methods involving relevant structure feature sizes below 100 nm are referred to as nanotechnology and fabricated layers in the same thickness regime are referred to as thin films. Material patterning, addition or removal are used to realize physical structures, and etching, lithography, deposition, annealing, bonding, milling and printing are all established microfabrication techniques. These techniques are divided into various subcategories, but a few of them relevant for this work are reviewed here.

3.1 Electron Beam Lithography

Electron beam lithography (EBL) is a common method to produce very precise single-digit nanometer structures and patterns with an electron beam writer (EBW)^{67,68}. The operating principle of the tool is similar to the SEM. In EBL an electron-sensitive resist is applied on the substrate surface. A high-voltage electron beam is used to scan over the sample pixel-by-pixel and the radiation dose received from the electron beam exposes the resist film, changing its solubility. The exposed area is more soluble, and patterns are created by selective removal in the developer solution. The process is completely photomaskless.

The resist is mainly exposed by the secondary electrons that have a lower energy than the incident beam. Due to the secondary electrons being scattered in a slightly wider area than the incident electron beam, the patterns on the resist are slightly broadened. This so-called proximity effect near the writing area, can cause an undesired widening of the patterns, but most commercial EBL systems have proximity effect correction (PEC)⁶⁹ software tool for optimizing the beam dosage in critical areas. The pattern spreading can also be avoided by giving the electrons less chance to scatter from the matter by thinning the substrates. The resolution of the EBL is primarily determined by the scattered electrons in the resist and substrate⁷⁰.

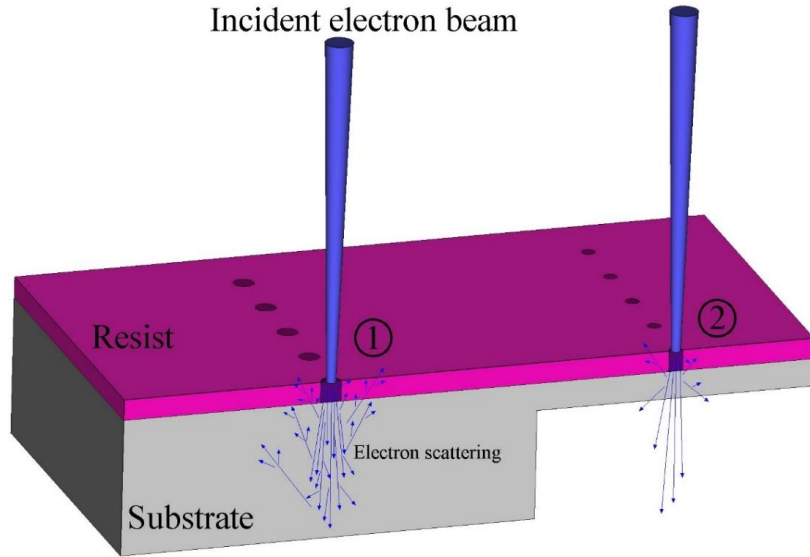


Figure 10. Electron beam lithography. Incident electron beam exposes the electron sensitive resist by changing the resist solubility. (1) Electrons scattering back to the surface from the substrate exposes the resist. The proximity effect widens the patterns. (2) Thinner substrates let more electrons pass through the resist and the substrate, causing less proximity effects.

In general, EBL is referred to a direct writing method capable of producing custom patterns. As a very fine probe is used for exposures, the throughput can be very low. Higher throughput tools may use shaped beams, that are produced by placing a shaped aperture in front of the incident beam⁷¹. A laser stage can be added to the system for more precise writing. EBL works very similar to SEM, and in many EBL tools the electron beam is also used for low resolution imaging and with a help of image recognition to locate the alignment markers on the sample. Due to slow writing speeds, EBL systems are not practical for production, but are mainly used for prototyping, photomask writing for very large-scale integration (VLSI)^{72,73}, small batch production and stamps for nano-imprint. The advantage of EBL is the possibility to write multiple designs on a single substrate.

3.2 Chemical Vapor Deposition

Chemical vapor deposition (CVD) is a common method in semiconductor technology and can be used in film deposition and surface treatment. A wide range of materials and film morphologies can be deposited by changing precursors, temperature, pressure, gas flow, reactor geometry, substrate surface area and substrate morphology^{74,75}. Typical grown layers are silicon dioxide, silicon nitride and polycrystalline silicon. In CVD the deposited films are formed in a vacuum by chemical reactions. Precursors react in the gas phase and forms a solid film on a normally heated substrate surface⁷⁴, for instance:



As the introduced precursors are gaseous, they deposit on all open surfaces and permeate reasonably well on trenches and narrow pinholes. The reaction chamber walls gets covered as well. Preferably, the reaction is activated at the sample surface and not during the gas phase, as the gas phase nucleation leads to a dust aggregation. A typical CVD processes enable uniform thickness and low porosity⁷⁴.

3.3 Physical Vapor Deposition

Physical vapor deposition (PVD) differs from chemical vapor deposition (CVD) in that PVD is based purely based on physical phenomena. PVD allows a wide range of materials to be deposited and common applications include thin films for semiconductors^{76,77}, improving wear behavior, anti-reflection coatings⁷⁸ and corrosion protection⁷⁹. PVD can be categorized into two main methods which are evaporation and sputtering^{80,81}. In evaporation, the target material and sample are facing each other in a vacuum. To ensure the evaporated atoms will not be scattered around with the gas in the vacuum chamber before hitting the sample surface, the chamber must be pumped typically below 0.01 Pa pressure⁸². High temperature is applied by resistive heating with a filament, or by an electron beam. When the material begins to evaporate or sublime, the detached material is hurled in straight lines, until hitting on the vacuum chamber wall or sample surface. Evaporation forms smooth non-conformal and columnar⁷⁹ layers that might be less dense than the target material. With increasing deposition energy the PVD coatings tend to grow smoother and denser⁷⁹.

Sputtering, on the other hand, is performed at higher pressure (0.1-1 Pa). Argon plasma is created between the sample and target metal by ionization of pure gas, and is confined by a magnetic field around the target. Argon ions hit the target material and ejects atoms or atom clusters from the target, which are condensed on the sample surface. As the sputtering target is rather large and close to the substrate, the results is a more conformal film. Films deposited by sputtering have similar properties as the target material. Sputtered coatings exhibit a dense and fibrous⁸³ structure. In connection with sputtering, it is possible to use reactive gases to form oxides and nitrides of the deposited metal films.

3.4 Atomic Layer Deposition

Atomic layer deposition (ALD)^{84,85} is a special case of CVD. Instead of simultaneous introduction, two precursor gases are pulsed one at a time on the surface, so that the purging pulse of inert gas is introduced between each precursor pulse. In each precursor gas pulse there is plenty of gas in the chamber to ensure that all the sample surface gets covered with the gas (Figure 11a). The process is self-limiting in a way, that the chamber conditions enable the sample surface to absorb a single atomic or

molecular monolayer from the precursor gas. When all surface sites have been covered with a monolayer, and no more reactions can take place, the chamber is flushed with an inert gas (Figure 11b). The second pulse takes place (Figure 11c) where the new precursor gas can react with the previous layer to form a monolayer of the second material. Once the excess second precursor gas has been flushed, one cycle has been finished (Figure 11d). The grown layers are either amorphous or polycrystalline. Growing of III and V semiconductors and epitaxial layers with ALD has recently become more popular⁸⁶⁻⁸⁸. Changing of the deposited film material is easy by just changing the precursor gases.

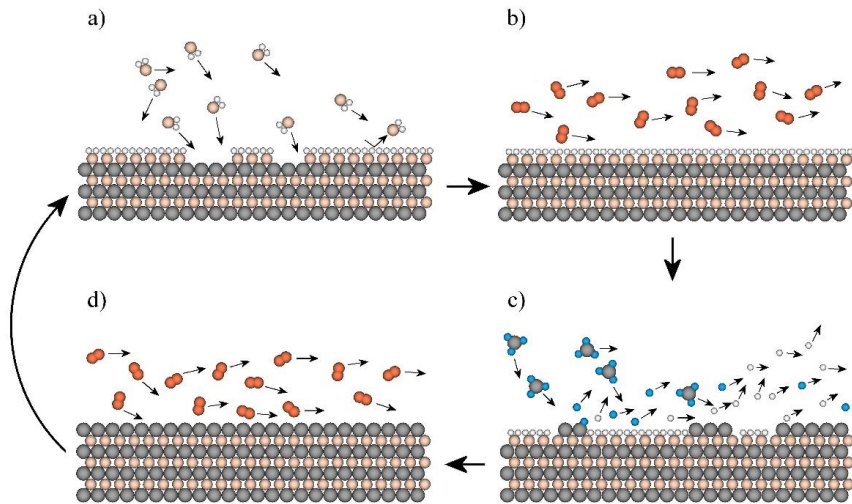


Figure 11. A generic ALD film growth cycle, with two precursor gases. a) First precursor gas is introduced and absorbed to the surface forming a monolayer. b) Purge with inert gas. c) Second precursor gas is introduced and absorbed into the surface forming a second monolayer. d) Purge with inert gas. In one deposition run the cycle (a-d) is repeated N times.

Once introduced, the abundant precursor gas reaches the complete surface coverage of the sample, and permeates well even into the deep trenches and very thin holes. The thickness of the film is controlled by the number of cycles, and not by the locally available gas as in the standard CVD.

As the pulse length does not dictate the reaction or growth rate, all locations on the surface are covered with the same thickness layer (Figure 12). Monolayer-by-monolayer growth enables covering narrow cavities and pinholes. This might not be the case with regular CVD, where the film keeps growing closest to the gas source. This way, the precursor gas may not reach the bottom of the pinhole at all before depletion at the pinhole neck. This has been the primary incentive to use ALD to cover the pinholes as discussed in Publication III.

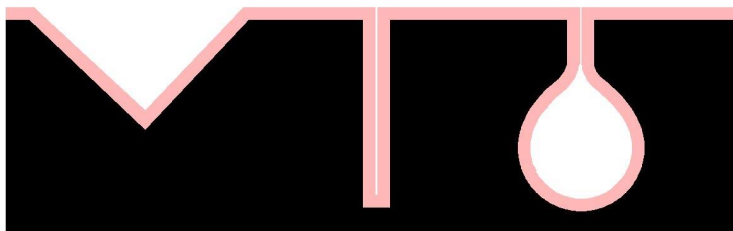


Figure 12. ALD film thickness profile over various surface topographies.

3.5 Metallorganic Vapor Phase Epitaxy

Metallorganic vapor phase epitaxy (MOVPE)^{89,90} is a semiconductor growth method that relies on reactive gases that react at the surface. MOVPE is often compared with molecular beam epitaxy (MBE), as these two epitaxial methods can grow III and V semiconductors. The method is widely used to form single-crystalline nanowires. The MOVPE process takes place at atmospheric or at a moderate pressure of 10 – 50 mbar⁹¹ in comparison to the vacuum condition used in PVD. The precursor organo-metallic gases are combined with the carrier gas and are introduced to the process chamber. Instead of the cyclic gas introduction used in ALD, in MOVPE constant gas flow is applied. The gases are absorbed on surface, undergo pyrolysis and the decomposed subspecies are incorporated into the epitaxial layer. The growth rate is typically slow, but is faster than that of ALD or MBE. The growth rate can be enhanced locally by introducing liquid metal nanoparticles (NPs) on the sample surface. As MOVPE is good for growing III-V semiconductors, but have limited control over the monolayers, MOVPE have limited applications in industry.

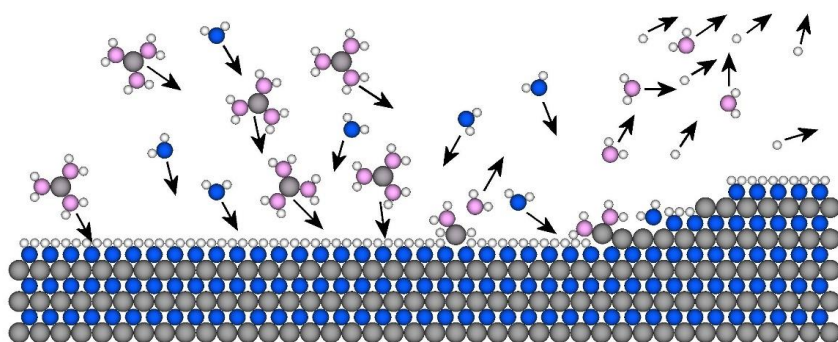


Figure 13. Schematic of the MOVPE process. Precursors are absorbed by, into sample surface and after pyrolysis the decomposed subspecies are deposited on the epitaxial layer. Waste products are exhausted into the vacuum.

3.6 Vapor-Liquid-Solid Mechanism

Vapor-liquid-solid (VLS) is a nature mimicking process that enables accurate control of the dimension, location, composition and chemistry of NW materials^{92,93}. VLS mechanism can lead into growth of one-dimensional (1D) structures as vertical pillars or 2D ribbons in a horizontal growth direction on a flat sample⁹⁴. The VLS process was proposed in the 1960's by Wagner⁹⁵⁻⁹⁷ and is the most common bottom-up, self-assembly NW growth method. The method was refined to nanoscale dimensions in the 1990's^{98,99} and single-walled carbon nanotubes (SWCNT) down to 1 nm in diameter can be synthesized. NW morphology and optical properties can be adjusted by process parameters, such as growth time, temperature, gas flow, catalyst NP size and NP density. The diameter of the single crystal rod-like NW is determined by the catalyst NP. MOVPE is a popular method used to facilitate VLS nanowire growth. VLS is a theory that explains nanowire/nanotube growth on a catalyst, where the precursors are introduced in gas phase and form a solid on the heated substrate. The precursor gas decomposes in the chamber due to heating or collisions in a plasma. Metallic catalyst nanoparticles (mostly Au) deposited on the substrate are assumed to be in liquid state¹⁰⁰ when the precursor gas atoms (e.g. Si from Si precursors or C from carbon precursors) diffuses through the liquid catalyst and forms a solid single crystal on the liquid-solid interface under the catalyst NP. The catalyst particle is effectively lifted upwards by the growing NW under it. VLS applications are to be found in optoelectronics¹⁰¹, quantum devices⁹², surface-guided planar nanowires¹⁰², optical sensors and have sparked interest in the renewable energy sector¹⁰³.

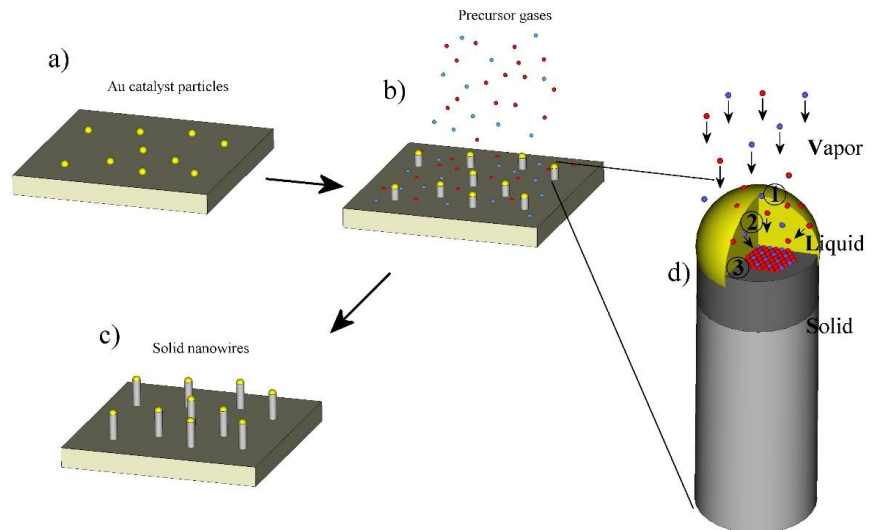


Figure 14. Schematic diagram of a generic VLS process. a) Au catalyst particles are deposited on the sample surface. b) Precursor gases are introduced and absorbed into the catalyst. c) Solid single-crystal nanowires formed on the surface. d) (1) precursor is decomposed at the catalyst surface and (2) is diffused through the liquid catalyst (3) crystallizing into a solid nanowire.

3.7 Reactive Ion Etching

The above mentioned CVD, PVD, ALD, MOVPE and VLS processes are material additive. There are several ways of removing material, and etching is one of the most common methods in micromachining. Several dry-etching methods exist, and reactive ion etching (RIE)¹⁰⁴⁻¹⁰⁹ is an intensively used method in the microelectronic industry to etch a wide range of semiconductor materials with a variety of selective etching chemistry. In microfabrication for large volume, material removal by dry etching, like RIE, is a preferred method. In RIE the etching gas is released into the chamber, and a radio frequency (RF) 13.56 MHz powered cathode is used to ignite the plasma. Partly ionized plasma contains equal amounts of positive ions from the broke-down gas and negative electrons. Typical silicon etching gas CF_4 is broken-down by RF mostly into ions CF^{n+} ($n = 1-3$) and a small amount of F^- . There are also neutral free radicals CF_n ($n = 1-3$), which can be excited to CF_n^* ($n = 1-3$). The positive ions are accelerated by the electric field and bombard the cathode and sample surface. Free radicals diffuse in the chamber and reach the sample surface. As a result of chemical reactions between the radicals and etched material, volatile neutral compounds CFSi_3 , CF_2Si_2 and CF_3Si are created and removed from the chamber. F^- ions are trapped on the top electrode and try to lose an electron or recombine with CF^{n+} to form neutral radicals F and CF_4 . The neutral radical species are responsible for isotropic etching. Only the positive ion species contribute to directional bombardment. Positively-charged plasma ions are accelerated towards the cathode by an electric field created by the same electrodes that ignite the plasma, which is a typical capacitively-coupled plasma (CCP) RIE setup. The plasma and cathode are not in direct contact and are separated by the so-called dark space. The bombardment of energetic ions heats up the cathode.

Etching the side-wall profile can be improved by dropping out the reactive chemicals, but the result is a slower etching rate¹¹⁰. The polymers and photoresists typically used for the pattern replication in RIE are temperature sensitive, and thus the increased temperature of 100-200 °C¹⁰⁸ caused by the bombardment at the substrate causes PR deformation¹¹¹. Thus power input and etch rates are limited by the PR thermal stability.

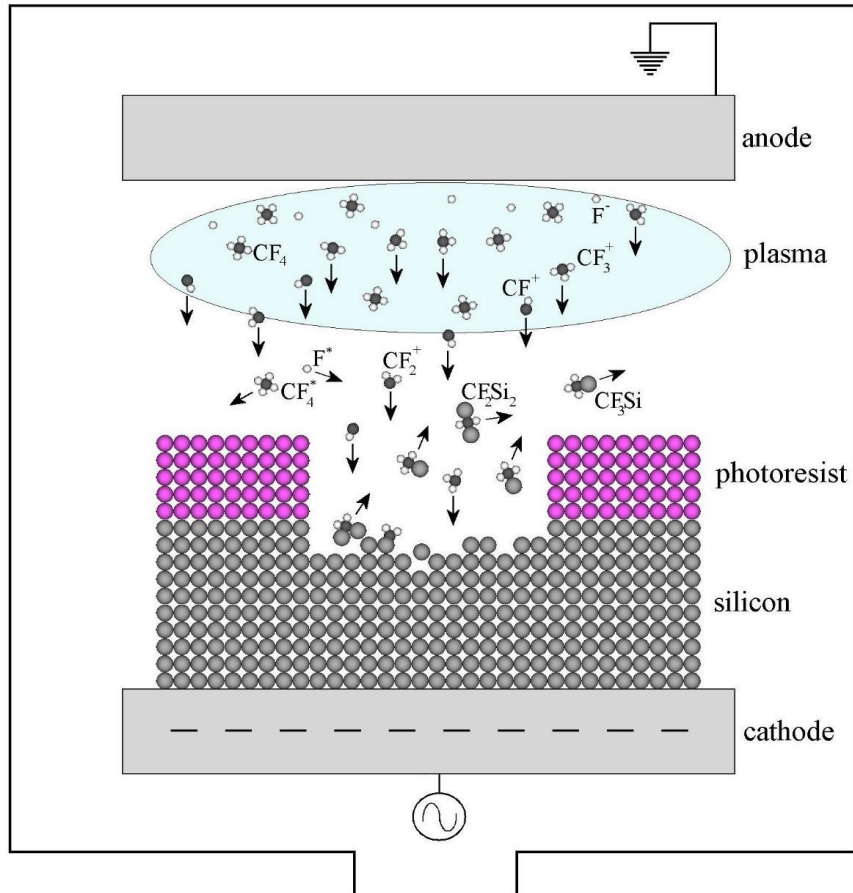


Figure 15. A diagram of a generic RIE setup and a standard silicon dry-etching process. The photoresist is patterned by lithography and the silicon surface is exposed for etching on the locations where the resist is removed by the developer.

A special case of RIE is deep-reactive ion etching, or DRIE. Two inductively-coupled plasma (ICP) variants are used in DRIE, cryogenic RIE^{112,113} and Bosch¹¹⁴. In an ICP system the potential used to generate plasma and to accelerate ions can be individually controlled. Bosch is a cyclic process in which HAR of the etching can be achieved. DRIE is mainly used for anisotropic etching to realize vertical side-wall profiles, due to the directional ion bombardment.

4. Results and Discussion

This chapter includes an overview of the research that has been carried out utilizing the charged-particle beams and fabrication processes described in chapter 3. FIB processing has played an important role in research and has been utilized in most of the research carried out.

Milling, etching and deposition are established micro- and nanofabrication techniques. These techniques are applied on silicon wafers on a regular basis, as silicon is the most commonly used substrate material. Depending on the tool, the maximum processed surface area can be achieved in either a wafer- or cassette-scale process. Serial-mode process methods work much better for prototyping, and perhaps for very small batches. In addition to the imaging and analysis methods discussed in this thesis, FIB offers alternatives for the above mentioned fabrication techniques. FIB is a serial writing tool and the ion beam can be used for direct patterning, which is simpler and requires fewer process steps than conventional microfabrication methods; however it has drawbacks. As the beam is focused on a single tiny spot, true parallel processing is excluded, which makes FIB processing slow¹¹⁵ in comparison to many conventional fabrication techniques that rely on parallel patterning and etching.

4.1 Silicon Nitride Membrane Device Platform Fabrication

Silicon nitride has good physical and chemical properties, which is why it is widely used in the microelectronics industry. A technique to perforate a thin 100 nm free standing SiN_x membrane with an FIB was developed and described in publication IV. The developed technique was then used to perforate a commercial SiN_x membrane suspended by a silicon frame (or window) so that an environmentally isolated device platform suspended on four narrow bridges for low temperature physics applications was realized. The low temperature physics devices are extremely sensitive to environmental thermal noise, and bridges suspending the platform improve the thermal isolation, in comparison to full non-perforated suspended membranes^{116,117}.

A standard device fabrication method to perforate the SiN_x membrane would be to use RIE, but this method would require masking and lithography steps that are incompatible with the sensitive device fabricated earlier on the platform. Likewise,

low-temperature devices cannot be fabricated on perforated membrane, as the standard fabrication methods, such as photoresist coatings would not work in an intended way. The best alternative is to first fabricate the device with signal wires on the membrane and then to perform a delicate membrane perforation in a subsequent step.

As the FIB process involves bombardment of charged particles and the isolating SiN_x membrane has a low I_{SC} , there is a heavy charge accumulation visible on the blank membrane (Figure 3b). SiN_x membranes with thin and large area cannot withstand the heavy charging induced by the ion-beam milling, which makes the membrane buckle and inevitably break. It was noted that local charging caused by ion-beam milling is also detrimental, and responsible for tearing the membranes, or breaking them completely. A 0.92 nA ion-beam current is used to perforate the membrane, as smaller beam currents are ruled out for being considerably slower, and they do not provide any significant reduction in charge accumulation. When charging has been alleviated by increasing the I_{SC} with charge-conductive structures, in this case with a 30 nm-thick copper mesh, the buckling and shattering of the membrane is reduced dramatically, thus allowing a successful perforation.

Once the charging issue was resolved, the second obstacle was to overcome the stress. Silicon nitride membranes are well known to carry residual tensile stress (RTS)¹¹⁸⁻¹²⁰, originating from the high temperature fabrication process of SiN_x . The accumulated stress is in proportion to the differences in the coefficient of thermal expansion (CoTE) of the SiN_x membrane and the substrate (or any adjacent layer) and ΔT (ΔT is the temperature difference of SiN_x deposition temperature and the room temperature). When a stressed SiN_x membrane is being weakened in one direction by the FIB milling, the stress in the whole membrane is relaxed when the membrane breaks partially or completely (Figure 16). The stress release becomes apparent, when the thin SiN_x membrane is unevenly released from the edges of the suspended membrane window, as the pulling forces applied on the membrane from the surrounding bulk tear the whole membrane in half.

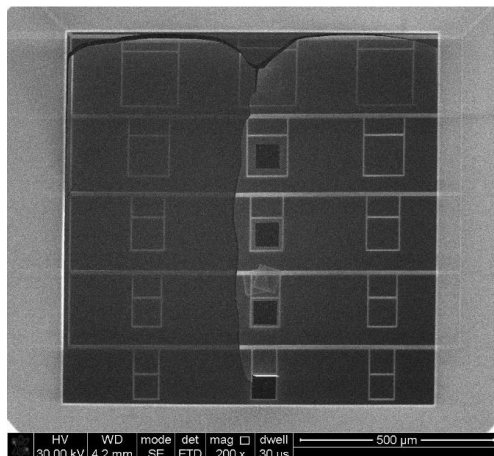


Figure 16. A Micrograph of a broken 1 mm² size SiN_x window after FIB milling. A poor choice of milling strategy results in a partial or complete breakage of the SiN_x window. The milling has progressed to the largest test pattern on the center column, where the membrane has started to break and a faint milled rectangle is visible inside the test pattern.

4.1.1 Charge Cancellation

Fabricating devices, such as tunnel junctions, require metal evaporation and EBL process steps. Commercially available 1 x 1 mm² silicon nitride membranes are spin-coated with photoresist, and exposed in standard EBL steps. The exposed sample is developed and covered in an evaporated thin metal coating. In the following lift-off step, the undeveloped parts of the resist are removed by stripping. The metal located on the top of the dissolved resist is also removed, leaving behind the metal pattern that was written with EBL. This process is repeated until the desired device design is achieved. Conducting copper wires are fabricated in conjunction with the final device fabrication step on the membrane thus saving in processing steps and time. The copper wires on the membrane provide guidelines for milling the platform and bridges, as well as for the release milling strategy.

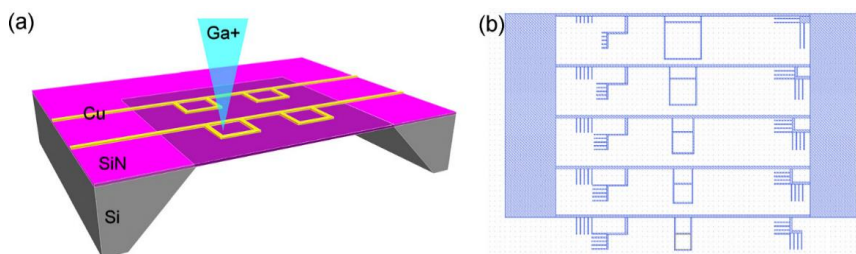


Figure 17. a) Gallium ion beam (blue) is used to perforate the free-standing silicon nitride film (purple) according to copper mesh (yellow). b) Layout for testing three different milling pattern designs with five varying separation distances. [Publication IV]

To save time in the EBL writing step, a minimal amount of patterns that are sufficient for FIB perforation are drawn. This requires a decision on finding the most efficient

mesh pattern for charge removal. Three design proposals were tested, based on the past experience of similar structures. Several test patterns are milled, and the results are shown in Figure 18b.

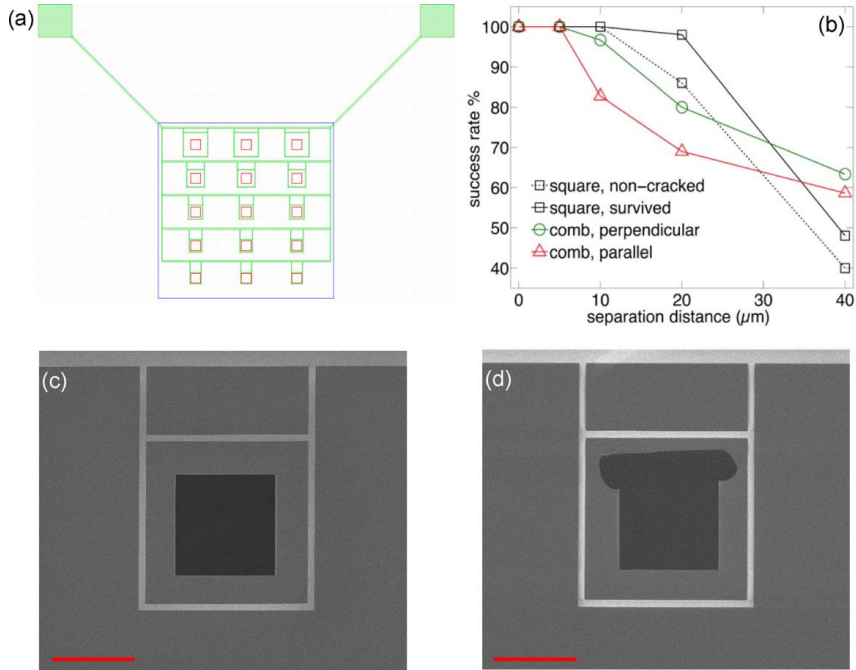


Figure 18. a) A layout for a tested square pattern mesh. Excess charging from the mesh on the membrane is wired to the larger pads outside the membrane. b) Results showing success rates as a function of separation distance for each tested mesh pattern. c) A successful cut on a square copper mesh. d) An unsuccessful cut on a similar copper mesh. The scale bars are 50 μm . [Publication IV]

The maximum distance the successful milling can be performed from the nearest wire is tested in conjunction with the patterns tested and is defined as a separation distance. A 60 μm rectangle hole is milled in the center of each test pattern. According to the results in Figure 18b, the square pattern is effective up to a separation distance of 20 μm , whereas the comb patterns are not that effective and start breaking already after a separation distance of 5 μm .

4.1.2. Stress Cancellation

The uneven perforation of the SiN_x membrane results in inevitable breakage, due to inherent stress. A perforation strategy discussed in Publication IV demonstrates a gradual release of the bridges and the platform that enables fabrication of free-standing suspended SiN_x film device platforms by FIB milling as a final process step. It was found that the 100 nm thin SiN_x membrane of the size of 1 mm^2 can withstand a maximum rectangle hole size of 60 by 60 μm^2 without tearing. Any larger hole milling without stress reduction steps would tear the membrane, 200 μm size hole being an absolute maximum. In a stress-mitigation milling strategy, the SiN_x window is first

released from the supporting silicon frame by milling the red squares (Figure 19a) evenly from all sides, before moving to the inner 60 μm sized rectangles.

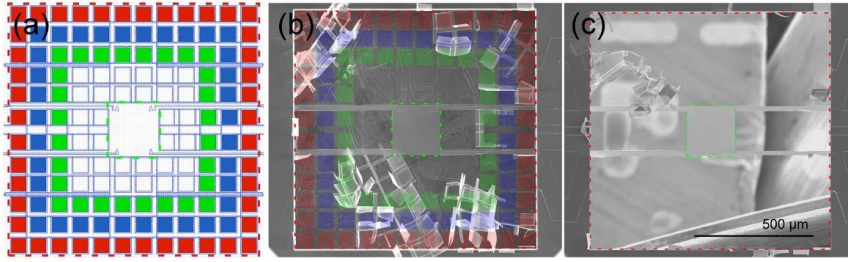


Figure 19. a) Stress-mitigation perforation strategy. b) A false color micrograph of an almost completed milling showing the milling strategy and some membrane fragments. c) A completed released free-standing device platform suspended on four bridges. [Publication IV]

4.2 Device Fabrication By FIB Surface Doping

In Publication VII it is shown that a gallium ion beam can be used to passivate a silicon surface to form an HAR structure by DRIE. As described in chapter 2, gallium penetrates a few tens of nanometers into the silicon forming a surface layer, which can act as an efficient masking layer for standard silicon wet¹²¹ and dry etching. For a typical structure a sufficient etch masking for one device can be achieved in seconds. The masked layer is then further processed with DRIE which will remove silicon from the unmasked area. The parallel etching mode of DRIE is able to reliably remove larger volumes, doing so much faster than could have otherwise been achieved using ion beam milling¹¹⁵. A typical milling rate for FIB is 0.1 [$\mu\text{m}^3/\text{min}$], and a typical etching rate for DRIE is 2 [$\mu\text{m}/\text{min}$], which means that for any larger surface area removal the parallel mode of DRIE is orders of magnitude faster. Least processing time is required when FIB doping is used as a dark field mask, where least area has to be protected by gallium doping and most material is removed by DRIE. The combined FIB-DRIE method is ideal for various prototyping or small batch processes as the resource consuming steps have been reduced to a minimum.

The masking of 3D structures with any degree of morphology is nearly impossible by conventional lithography steps. The direct doping of the device surface by the gallium beam by-passes the lithography step, and is entirely maskless. A suspended thermal actuator (Figure 20) is modified by surface doping of gallium (Figure 20b) to define the target structure, after which the unmasked silicon is etched with DRIE (Figure 20c). The doses for protective gallium doping have been defined earlier by Chekurov et al.¹²², and a sufficient dose is achieved in 400 s with 9.7 pA for the shown bridge structure of 100 μm x 0.5 μm .

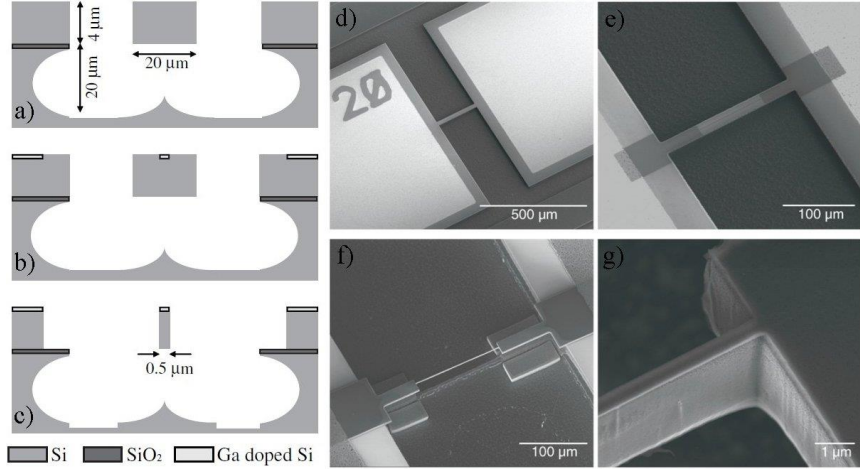


Figure 20. Process steps for modifying a ready-made thermal actuator. a) Schematic of the unmodified thermal actuator cross-section. b) Doping of the thin surface layer by FIB. c) DRIE etching of unmasked silicon. The BOX layer prevents further vertical etching. d) Electron micrograph of unmodified actuator e) electron micrograph of actuator after gallium doping f) electron micrograph of DRIE-etched actuator and g) higher magnification of the actuator after modification. [Publication VII]

As the bridge is much thicker than the thin surface amorphization, the gallium beam radiation does not have any measurable impact on the electrical properties of the microactuator. The IV behavior and power-resistance characteristics correspond to typical silicon microbridge actuators. The measured power-resistance behavior of the FIB-DRIE fabricated microbridge corresponds to a typical microbridge actuator power-resistance curve by exhibiting a characteristic resistance peak of R_{peak} when enough heating power is applied (the peak is shown as a dashed line in Figure 21a). The power-resistance behavior is tested with microbridges that are unmodified, FIB milled or FIB-DRIE modified. The results show that independent of the fabrication method, the power requirements for maximum resistance are only dependent on the width of the bridge (Figure 21b).

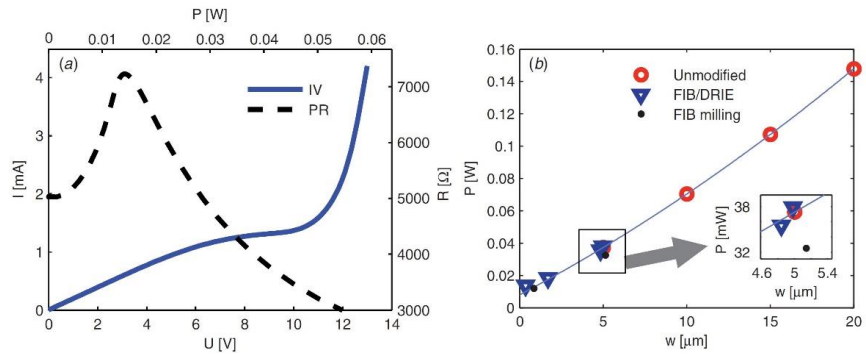


Figure 21. a) IV- and power-resistance curves of an FIB-DRIE fabricated $360 \text{ nm} \times 100 \text{ } \mu\text{m} \times 4 \text{ } \mu\text{m}$ size microactuator bridge. b) Peak power consumption [P] dependence on the microactuator fabrication method and the bridge width [w]. [Publication VII]

As proof of concept of the fabrication method, a real device was fabricated. A 100 μm long double-ended tuning fork resonator of 2 μm in width (Figure 22a) was processed with a combination of FIB-DRIE process. In parallel to the device fabrication, a COMSOL multiphysics modeling of the tuning fork was performed. In the model, the operational frequencies were $f_{\text{in-phase}} = 1.58 \text{ MHz}$ and $f_{\text{anti-phase}} = 1.66 \text{ MHz}$, and were found to be very close to the measured physical resonator frequencies $f_{\text{in-phase measured}} = 1.48 \text{ MHz}$ and $f_{\text{anti-phase measured}} = 1.62 \text{ MHz}$.

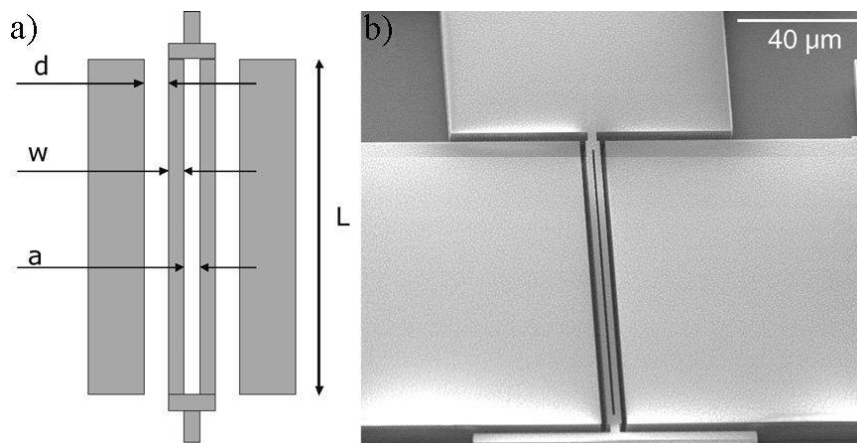


Figure 22. Double-ended tuning fork resonator. a) A layout with dimensions $d = 2 \mu\text{m}$, $w = 2 \mu\text{m}$, $a = 1 \mu\text{m}$, $L = 100 \mu\text{m}$, and height = $10 \mu\text{m}$. b) An electron micrograph of the realized resonator. [Publication VII]

The successful tuning-fork fabrication shows, that the FIB-DRIE method is sufficient for realizing real structures. The gallium masking combined with DRIE enables high resolution, fast and nearly effortless 3D micro- and nanostructures in an all-dry MEMS fabrication.

4.3 Nafion Film Characterization For Bio Sensor Applications

Nafion is a widely used polymer because of its physical properties and exceptional ion conductivity properties¹²³⁻¹²⁵. In electroanalytical applications, Nafion filtering and stabilizing¹²⁶ properties are of extreme interest. Of particular interest are the analytes that are being trapped inside the material. The structural information of Nafion thin films used in biosensor devices could explain how the sensitivity is lost and would also allow for the optimization of the selectivity between the analytes. Since its discovery in the early 1960's, one may find more than 33,000 references to Nafion in the DuPont database alone¹²⁷, and yet the fine structure of Nafion and its ionic conduction properties are still under heavy investigation. In publication I, Nafion morphology is shown in HR in 3D reconstructions. An improvement over earlier 2D and 3D imaging methods is achieved by UF staining and low-dose STEM tomography. The effects of film thickness and the combination with other elements are introduced in Publication II, where the customizability of Nafion is shown. The study discussed in

publication II is done especially having electrochemical sensors in mind. Nafion applied as a part of a blood-test sensor is discussed in Publication III.

Over the past six decades, a number of studies have been performed on the structure of Nafion (associated with fuel cell and catalyst applications mainly). For optimizing cation detection, interferent control, response times and permeability and other sensing properties, Nafion is often mixed with other materials, and is rarely seen as a pure sensor material. In the first part of the study of Publication II, a Nafion film is characterized in conjunction with tetrahedral amorphous carbon (ta-C). As ta-C is a well known material^{83,128,129} and attractive for electrochemical sensors, it is straightforward to study the electrochemical effects of a Nafion film deposited on the top of ta-C.

A layer of 20 nm thick titanium is sputtered on the top of a silicon substrate before the arc evaporation of 7 nm thick film of ta-C. After the wafer has been cut into smaller pieces, Nafion + DND suspensions of three different dilutions 5% wt-%, 1% wt-%, and 0.1 wt-% were drop casted on the top of the ta-C layer.

Cyclic voltammetry (CV) together with rotating disk electrode (RDE) measurements utilizing 1 mM $\text{Ru}(\text{NH}_3)_6^{2+/3+}$, $\text{IrCl}_6^{3-/4-}$ probes and uric acid (UA) show that the thin 0.1 % Nafion film already reduces the currents of the cationic species when compared to a bare ta-C electrode (Figure 23a). The current drops even further when 1 % Nafion is used (Figure 23b). A steady state is achieved at 3.6 μm thick 5 % Nafion film, where the cationic diffusion is controlled by the film thickness and used anions are filtered completely. Furthermore, the peak potential differences in Figure 23c show how well electrons can transport through the Nafion film. As the peak voltage differences $\Delta E_p = 67 \text{ mV}$ for 5% Nafion/ta-C and $\Delta E_p = 58 \text{ mV}$ for bare ta-C are so close to each others, it therefore can be deduced that ruthenium is enriched inside the hydrophilic channels of Nafion. As the peak currents are enhanced with increasing Nafion thickness, there is more ruthenium available for oxidation and reduction reactions. The increase of ΔE_p when the scanning speed increases is shown in Figure 24. At faster scanning speeds 5 V/s and 10 V/s, the ΔE_p decreases, and the reaction kinetics are faster. From this it can be concluded that ruthenium has no time to escape from the electrode surface and it is trapped inside the channels. Once the ruthenium is removed from the Nafion film with potassium chloride (KCl) flushing, the original function of the 5% Nafion film is recovered (Figure 23d).

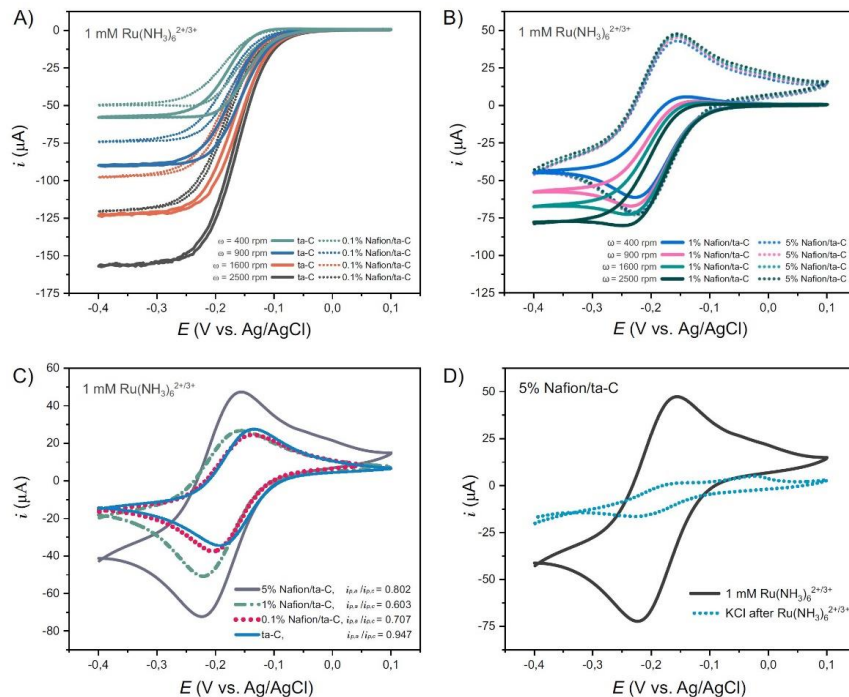


Figure 23. Electrochemical behavior of Nafion/ta-C films. Hydrodynamic voltammograms of a) bare ta-C and 0.1% Nafion/ta-C in $\text{Ru}(\text{NH}_3)_6^{2+/3+}$ b) 1% Nafion/ta-C and 5% Nafion/ta-C. c) Response and peak currents ratios for 5% Nafion, 1% Nafion, 0.1% Nafion and bare ta-C electrodes. d) 5% Nafion/ta-C in 1 M KCl after $\text{Ru}(\text{NH}_3)_6^{2+/3+}$ cycling. [Publication II]

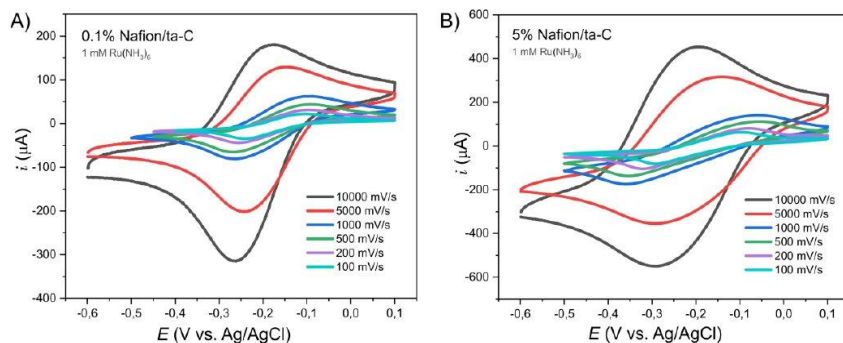


Figure 24. Cyclic voltammograms of a) 0.1% Nafion/ta-C electrode and b) 5% Nafion/ta-C electrode in 1 mM $\text{Ru}(\text{NH}_3)_6^{2+/3+}$ with different scan rates. [Publication II]

The CV measurement with $\text{IrCl}_6^{3-/4-}$ and UA analytes shows that even 0.1% Nafion coating effectively inhibit anionic diffusion through the film to the electrode (Figure 25a and 25c). Thicker 1% and 5% Nafion films reduce the flow of anionic species even further. This is an expected result as the negatively-charged anions are repelled by the negatively-charged Nafion channels.

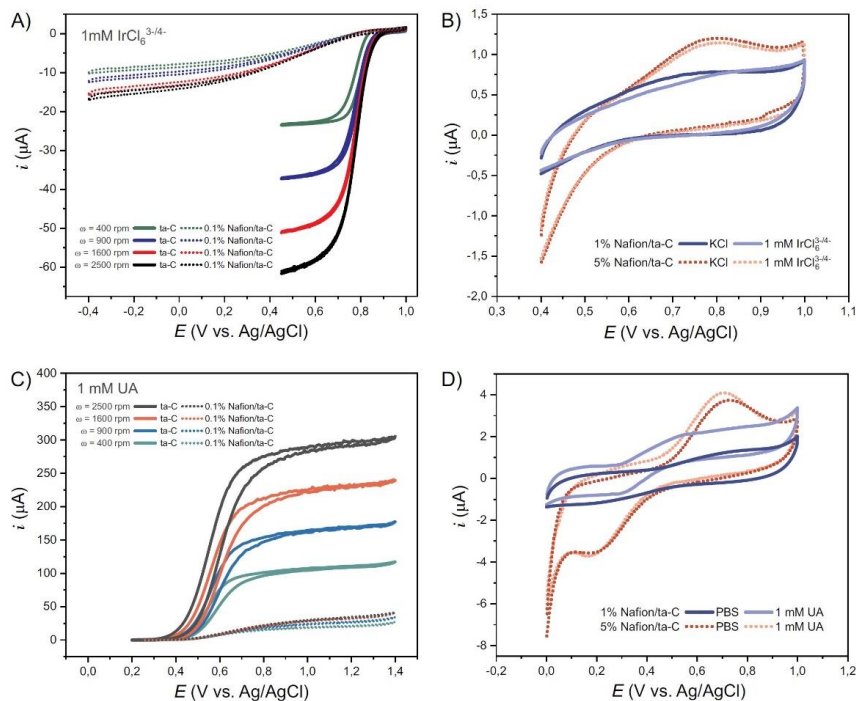


Figure 25. RDE results from $\text{IrCl}_6^{3-/4-}$ and UA probe measurements. Hydrodynamic voltammograms of a) 0.1% Nafion/ta-C in 1 mM $\text{IrCl}_6^{3-/4-}$ in KCl b) 1% and 5% Nafion in KCl and 1 mM $\text{IrCl}_6^{3-/4-}$ c) 0.1% Nafion/ta-C in 1 mM UA in PBS and d) 1% and 5% Nafion/ta-C in 1 mM UA. [Publication II]

Incorporating DNDs into Nafion/ta-C electrodes and using the same $\text{Ru}(\text{NH}_3)_6^{2+/3+}$, $\text{IrCl}_6^{3-/4-}$ and UA analytes, no significant difference in performance is observed with a 0.1% Nafion+DND/ta-C film compared to a 0.1% Nafion/ta-C film (Figure 27). This is a clear difference between a 5% Nafion+DND/ta-C film and plain 5% Nafion/ta-C film, as ruthenium and iridium probes both leak through the film with incorporated DNDs (Figure 27).

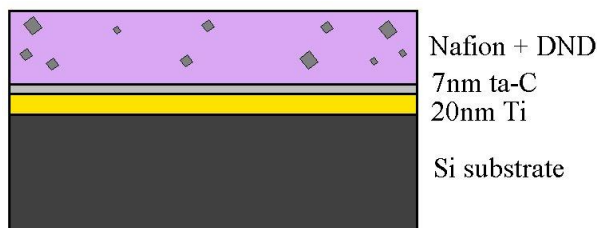


Figure 26. Schematic of the Nafion+DND/ta-C electrode structure.

The RDE measurements for the electrodes with $\text{IrCl}_6^{3-/4-}$ probes show the same behavior as with the $\text{Ru}(\text{NH}_3)_6^{2+/3+}$ probes above, and thus we can conclude that the electrodes have a similar performance (Figure 27a). The 5% Nafion+DND/ta-C, on the other hand shows a clear redox peak, meaning that the anionic iridium analyte is leaking through the Nafion film with carboxyl functionalized DNDs. However, further

studies are needed to conclusively determine whether the changes in permeability are due to the physical or chemical changes of the film.

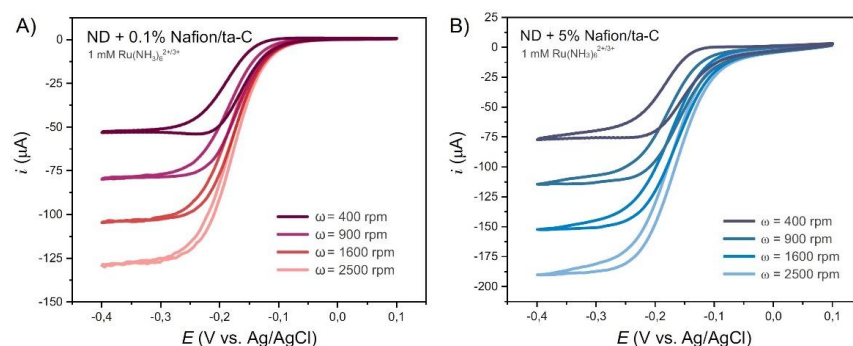


Figure 27. Hydrodynamic voltammograms for a) ND + 0.1% Nafion/ta-C b) Nd + 5% Nafion/ta-C in $1 \text{ mM Ru(NH}_3)_6^{2+/3+}$ in a 1 M KCl . $v = 50 \text{ mV/s}$ for all measurements. [Publication II]

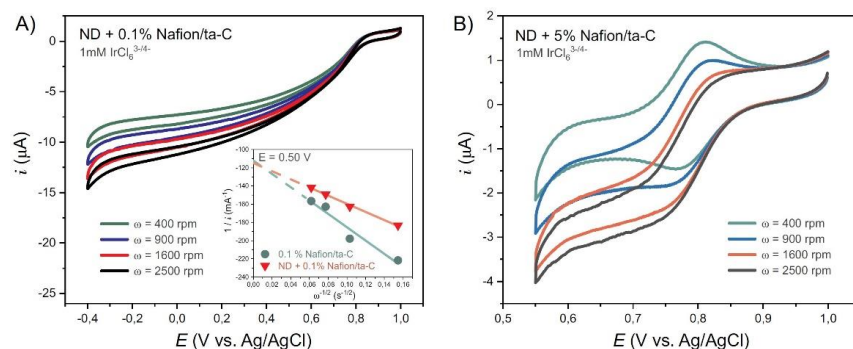


Figure 28. a) DND + 0.1% Nafion/ta-C in $1 \text{ mM IrCl}_6^{3-/4-}$ and 1 M KCl . Koutecký-Levich plot in the inset. b) DND + 5% Nafion/ta-C in $1 \text{ mM IrCl}_6^{3-/4-}$ and 1 M KCl . [Publication II]

The composite film selectivity for uric acid shows significantly different behavior, so that the selectivity to UA is lost, when DNDs are introduced into the film. Already the thin 0.1 % Nafion/ta-C+DND film selectivity for uric acid (Figure 29a) is completely different when compared to plain 0.1 % Nafion/ta-C (Figure 25c). The 5% Nafion/ta-C and 5% DND+Nafion/ta-C voltammograms are shown in Figure 29b. The introduction of DNDs into the 5% Nafion film, changes the chemical characteristics of the film. The chemical interactions in the film are observed as the UA enhances the redox peaks in DND-enhanced film (Figure 29b).

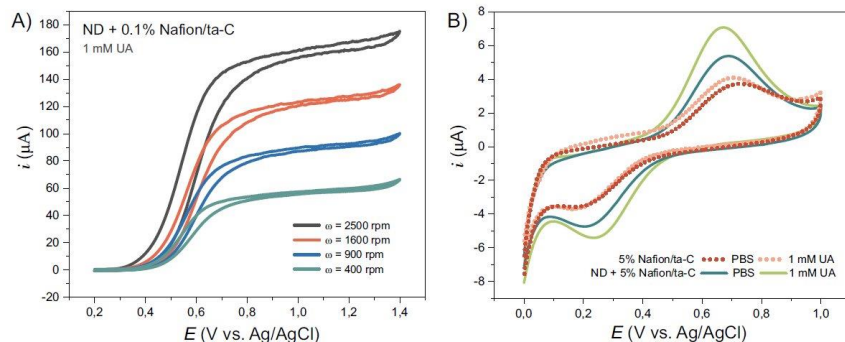


Figure 29. Cyclic voltammograms of a) DND + 0.1% Nafion/ta-C in 1 mM UA and b) 5% Nafion/ta-C and 5% DND+Nafion/ta-C in 1 mM UA in PBS. [Publication II]

From the above, it is established that carboxyl-functionalized DND affects the electrochemistry of thin Nafion films. The optimization of the film characteristics for specific applications requires a detailed analysis of the studied material. It is well established that the ion transport properties of Nafion are influenced by its morphology^{125,127}. Nafion is the most fragile and particle beam sensitive material to image with any known methodology. Thus it has been very hard to reveal its fine morphology for decades. Publication I shows the most advanced method for imaging the ultra-fine structure of Nafion so far. Uranyl formate (UF) negative staining is an established method in EM. In this study, the spin-coated Nafion thin films of thickness 10 – 100 nm are stained with UF, and the Quickie STEM tomography method is applied to these films. The advantage of using the Quickie method is that the radiation dose for the sample is only 26% of the conventional tomography done with two-degree increments, thus enabling the collection of sufficient amount of images for successful reconstructions. The utilization of 3 nm carbon coating for Nafion thin-film imaging has not been reported before in literature, and is contributing to the stable imaging in RT.

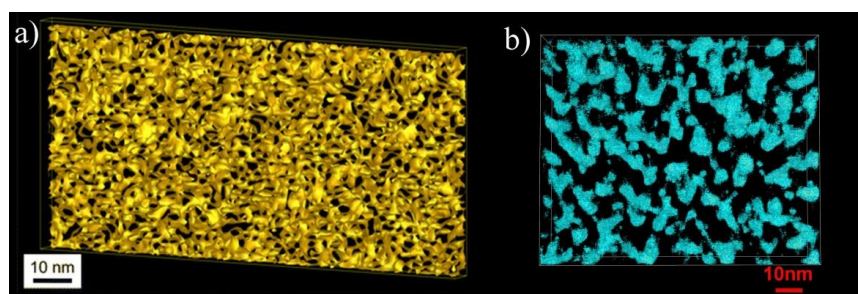


Figure 30. Comparison of the two most known EM reconstructions of Nafion fine morphology a) CryoET of hydrated as-cast Nafion channels by Allen et al.¹³⁰ b) STEM tomography of as-cast uranyl formate filled Nafion channels [Publication I].

The Nafion morphology revealed by the STEM tomography shows that the hydrophilic/hydrophobic phase ratio of Nafion 117 thin films is $\sim 0.3/0.7$ regardless of the film thickness. The channel diameter varies between 3 – 6 nm having some larger lumps randomly distributed. The channel thickness profile does not change between

different film thicknesses or within the film, and is similar in all studied films. The average channel distance within the film shows some distribution, centering around 12 nm for 10 nm films, 15 nm for 30 nm thick films, and 7 nm for 100 nm films. An interesting phenomenon of the cationic fiducial gold markers being attracted into hydrophilic Nafion pores is observed. This is an expected result as the positively-charged fiducial gold markers are highly hydrophilic and carry water within the ligand layer, so they are drawn to the negatively-charged sulphonyl group coated Nafion channels.

It is to be noted that the most well-known Nafion reconstruction by Allen et al.¹³⁰ compared with the presented STEM tomography results show different morphology (Figure 30), and no definite conclusions can be made from either of the presented methods. EM tomography is inherently susceptible to interpretation errors. There is no rule that would express the right contrast, brightness, threshold, or color conditions for tomography. The values for these parameters are chosen by experience, and are arbitrary to a certain degree¹³¹, i.e. no explanation are given for channel widths that are 1 nm and below and visible in Allen's reconstructions (Figure 30a).

Regardless of the detailed knowledge of the Nafion structure, the exceptional filtering properties of the material are highly sought after for real world applications. Publication VIII describes a disposable blood-test chip, where Nafion is used for selective detection of unbound acetaminophen concentrations in blood, by a simple dilution of the sample in PBS. SWCNTs that are produced by aerosol CVD^{132,133}, are press-transferred on a polyethylene terephthalate (PET) sheet in a roll-to-roll compatible method. Sensor patterns are transferred on the PET sheet by laser ablation to realize the electrode structures, and silver is screen-printed on top of the SWCNTs. The PET sheet is coated with 2.5 wt % Nafion 117, to functionalize the SWCNT layer in the working electrode. In the final step, the test strips are cut and covered with a poly(tetrafluoroethylene) (PTFE) film with a 6 mm opening at the electrode area.

The plain Ag reference electrode potential against the Ag/AgCl electrode stabilizes after 2 hours in 0.1 M PBS solution, whereas the Nafion-coated electrodes are immediately stable (Figure 31a). Also, a long-term study shows only a ~12 % potential drop for the Nafion-coated electrode over 7 days of operation in PBS, proving the potential of Nafion-coated electrodes. The susceptibility of the electrode to Cl^- by measuring the averaging potential of three Nafion-coated and uncoated electrodes is shown in Figure 31b. The potential linear dependency on a logarithmic scale over the Cl^- concentration suggests that the Nafion-coated electrodes can only be used in an environment with a known Cl^- concentration.

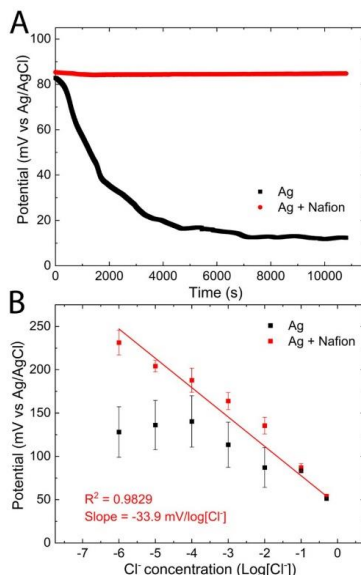


Figure 31. a) Potential stability of Ag and Nafion-coated Ag electrodes. b) Potential of Nafion-coated electrode is showing dependency of $-33.9 \text{ mV}/\log [\text{Cl}^-]$ of Cl^- -concentration. The non-coated electrode shows weak dependency. [Publication VIII]

Differential pulse voltammetry (DPV) measurements for acetaminophen in PBS, human plasma and whole blood, show an excellent linear relationship with increasing concentrations (Figure 32). The high correlation of DPV measurements indicates that the Nafion-coated electrode assay can rapidly detect unbound acetaminophen from the blood with a simple PBS dilution. The known protein anti-fouling properties of Nafion contribute to sustain the biosensors stability¹³⁴.

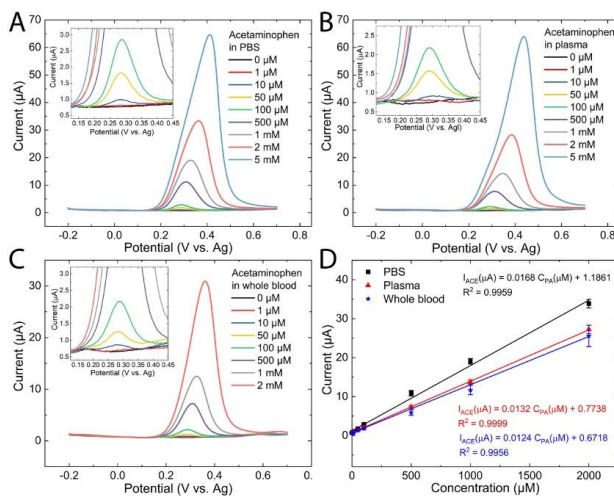


Figure 32. DPV measurements of increasing acetaminophen concentrations in a) PBS b) human plasma and c) whole blood. d) Results from all three measurements on a linear scale. [Publication VIII]

4.4 Surface Passivation By ALD Nanolaminates

A surface passivation with PVD and ALD coatings can significantly reduce the corrosion of steel^{135,136}. A corrosion protection of high-speed steel (HSS) by a standard PVD chromium nitride, enhanced by an ALD nanolaminate, is described in Publication III. Although PVD coatings are inherently more durable than soft ALD films, the disadvantage of such coatings is their porosity and non-uniformity. ALD films offer an optimal method for sealing the pinholes of PVD grown CrN (Figure 33). This happens due to the high penetration of the ALD precursor gas and conformal deposition on narrow and deep pinholes and trenches of differing morphologies¹³⁷. The CrN layer is sealed with an ALD-grown nanolaminate of alternating 5 nm thick layers of TiO₂ and Al₂O₃.

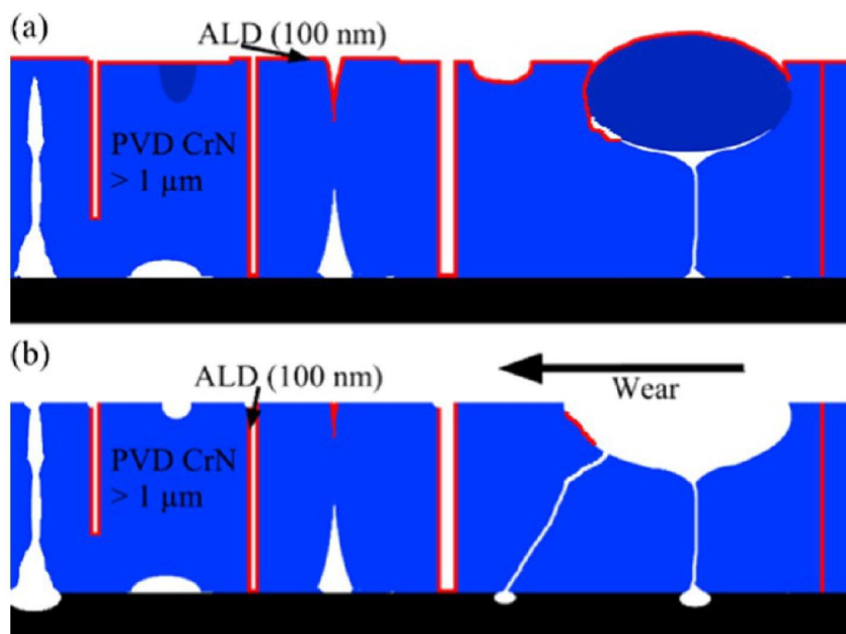


Figure 33. Schematic of PVD CrN/ALD coating on HSS. a) All open surfaces are covered with 100 nm nanolaminate, sealing pinholes and small voids. b) Mechanical wear removes the surface nanolaminate completely inducing additional damage and patch ways for corrosion, while pinholes remain sealed. [Publication III]

The passivation treated surface was exposed to alternating corrosion (salt solution of 0.2 M NaCl) and wear steps. The wear test was done with a ball-on-disk setup (Figure 34), and the last wear step was performed by grinding using a sandpaper. The FIB cross-sections were imaged with an SEM, and the images were used to determine whether the ALD coatings were used effectively to close the pinholes in CrN after the PVD growth. Linear sweep voltammetry (LSV) and LM were applied to observe the progress of corrosion.

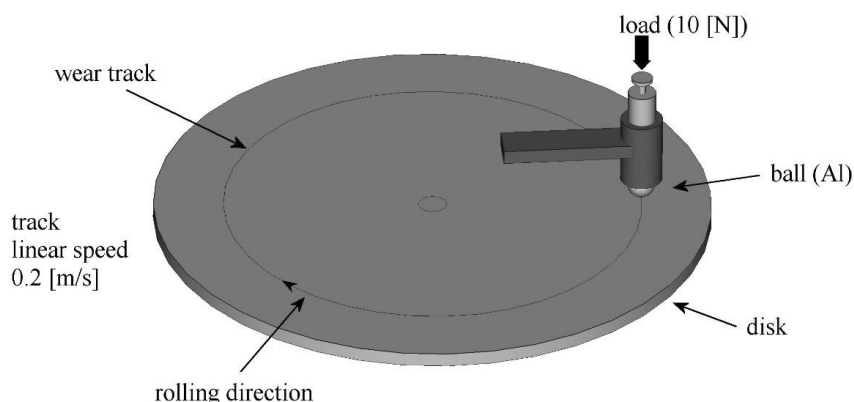


Figure 34. Ball on disk wear test configuration used for HSS.

The corrosion resistance of the PVD CrN-coated HSS is an order of magnitude higher than that of the plain HSS (Figure 35a). Coating the CrN layer with an ALD nanolaminate increases the corrosion resistance further by 2 orders of magnitude, but is reduced when the wear is applied to the surface (Figure 35b). At the end of the wear test, when the ALD layer is completely removed from the top layer, the corrosion current density of ALD/PVD-coated SSH is still less than half than that of PVD-coated HSS. The PVD-coated sample is approaching the corrosion potential and corrosion current density of plain HSS with increasing wear steps. The wear had a negligible effect on the electrochemical behavior of the PVD film, as the difference between the measurements of wear and no-wear samples are within the measurement variation. The LM inspection reveals that the plain HSS has already become completely rusted at the second wear step and getting only worse as the wear progresses.

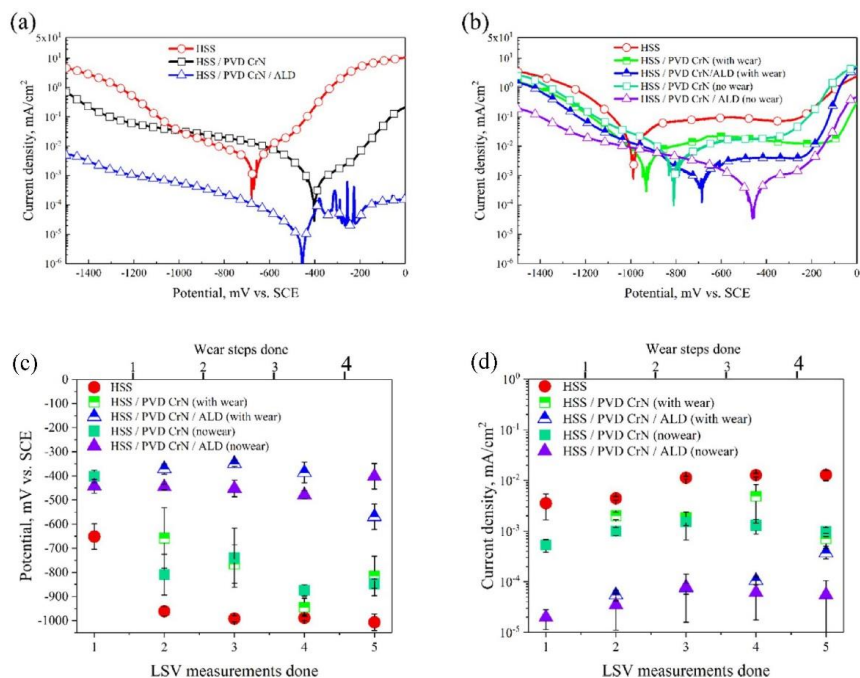


Figure 35. LSV measurements. a) Nanolaminate polarization curves before wear steps. b) 5 LSV measurements at different wear stages. c) All corrosion potential LSV measurement results. d) Corrosion current densities, with each point being an average of three LSV measurements. [Publication III]

The FIB cross-sections reveal that on the PVD-coated samples, the corrosion has progressed through all layers, and has reached the steel bulk (Figure 36). Some of the PVD coatings appear collapsed. Even under these circumstances, the corrosion current density in the hybrid PVD/ALD coating is half from the PVD coating alone.

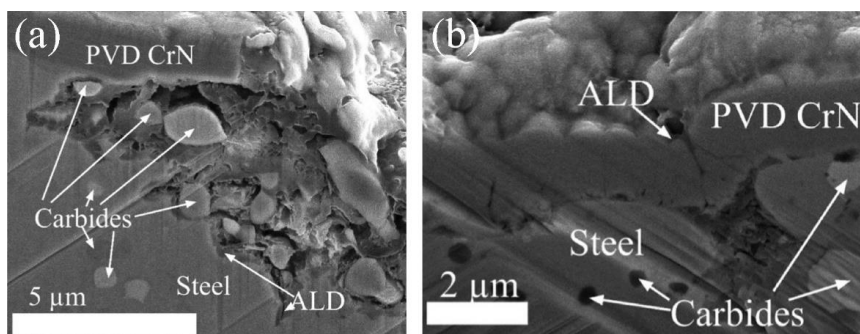


Figure 36. FIB cross-sections of PVD/ALD coating on SSH from two locations. a) Micrograph from the wear track, after all wear steps. b) Micrograph from a defect location outside the wear track, with only sand-paper wear. Both images exhibit some amount of diagonal curtaining effect from the FIB milling. [Publication III]

4.5 Copper Electrodeposition On Carbon Nanotube Fibers

Carbon nanotubes exhibit outstanding electrical conductivity, great elasticity and tensile strength. In combination with other materials, these properties can be optimized for a specific purpose or application¹³⁸. An electrochemical deposition of copper into a CNT fiber matrix to form carbon nanotube-copper composite wires is described in Publication V. The described method is stable, scalable and capable of increasing the electrical conductance of the bundle. The additional advantage is that the morphology of the original CNT bundle is retained, thus preserving the original properties of the bundle.

The CVD-produced nanotube fiber consists of various types of CNTs, and the final fiber bundle diameter varied between 5 and 30 μm . Electrodeposition was carried out by dipping the CNT bundles into an aqueous copper sulfate bath with a silver paste for the electrical contacts at both ends of the CNT bundles. A cathodic current of 0.06 to 5 mA was applied to the CNT bundles for 1 to 20 min to achieve a sufficient electrochemical driving force for copper nucleation and deposition.

FIB cross-sectioning and subsequent EDX measurements were carried out to analyze the distribution of copper within CNT-Cu wire and to investigate the copper growth mechanism (Figure 37). The ion-beam imaging shows (Figure 37a) that the Cu grains inside the wire are barely visible, while the Cu grain size on the exterior of the wire is in the scale of micrometers. This is an expected result as the copper ions in the solution have to first diffuse into the CNT matrix where they are depleted. It has been discussed earlier by Grujicic¹³⁹ et al. that a smaller copper concentration leads into smaller Cu clusters that are more distributed. It is assumed here that the low density of CNT bundle enhances the copper ion diffusion into the wire and increases the filling of the intertubular space of the nanotubes in the bundles. Despite the fact that CNTs are known to be hydrophobic, traces of sulphur revealed by EDX measurements shows that the aqueous electrolyte penetrates into the interior of the wire (Figure 37c).

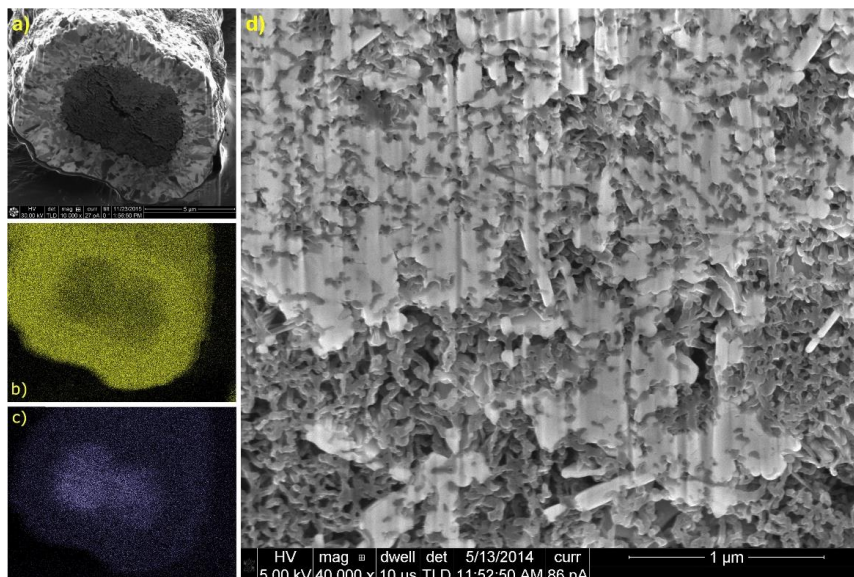


Figure 37. FIB cross-sections of the CNT-Cu wire. a) Ion-beam image. b) EDX map of copper. c) EDX map of sulphur. d) Higher magnification showing copper penetration. Copper (light contrast) has permeated deep into the core of the wire covering individual CNTs (dark contrast) and CNT bundles, with some voids. The vertical FIB milling curtaining effect is clearly visible. [Publication V]

As the copper cladding coverage on the fiber surface is dependent on the distance from the current feed point and advances along the length of the fiber, it is possible to determine the deposition rate for progressing coverage. The growth rate is dependent on the thickness of the fiber and growth current, and was found to be linear, being 0.08 mm/s at 1 mA for a 10 μm thick fiber (Figure 38).

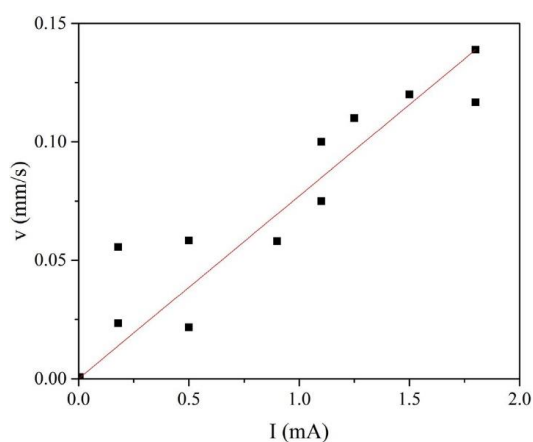


Figure 38. The deposition rates of 10 μm thick CNT wires at certain applied currents. Deposition speed v (mm/s) refers to the length of a continuous copper cladding on the wire surface measured after deposition. [Publication V]

The specific conductivity of the wire is found to be highest with the thickest Cu cladding and with the lowest CNT weight fraction (Figure 39). The most copper-rich wires approach the conductivity of pure copper, and are nine times higher than for the original CNT fibre. The resistance increases with an increasing CNT weight fraction and also when the Cu cladding layer is thinner.

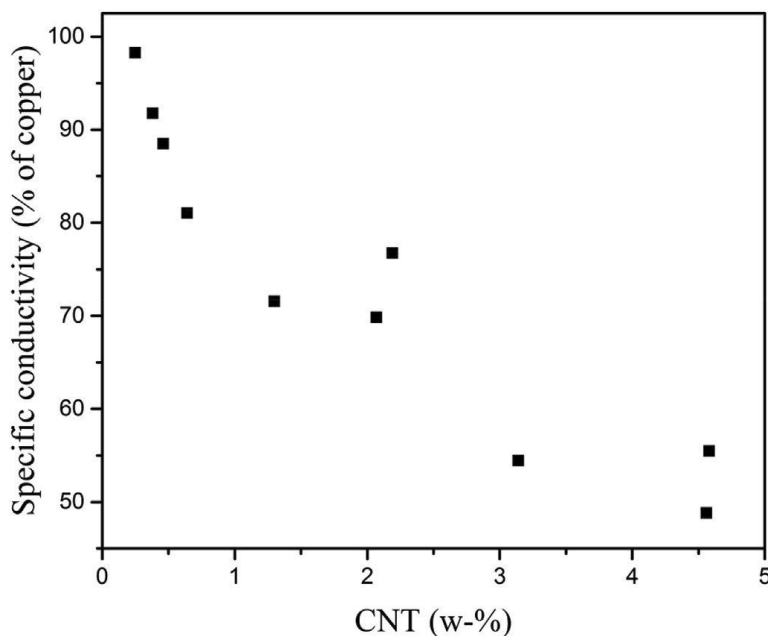


Figure 39. Specific conductivity of CNT-Cu wire at various CNT wt-%. [Publication V]

It is concluded that the increase in conductivity is mainly resulted from the thicker Cu cladding, as the composite wires with a thinner cladding and larger fraction of Cu inside the fiber have lower conductivity. The electron scattering in the grain boundaries is attributed to causing the conductivity difference. Another factor is the voids inside the bundle may be filling up with Cu with increased deposition time and may contribute to the conductivity increase.

4.6 Surface Treatment For Growing Nanowires

Two different methods to introduce nanowires on a single substrate are discussed in Publication VI, where controlled NW positioning and chemical composition on a single substrate are demonstrated. In separate growth steps, selective-area epitaxy (SAE) is applied to grow nanowires (NWs), which is then followed by catalytic growth of another set of NWs in a subsequent step. In the first NW-growth set, trimethylgallium (TMGa) and tertiarybutylarsine (TBA) precursors are used in the SAE and VLS-growth steps to obtain two types of GaAs NWs. Both types of GaAs NWs are grown side-by-side (Figure 40e), the latter VLS-grown NWs being slightly tapered and shorter in height.

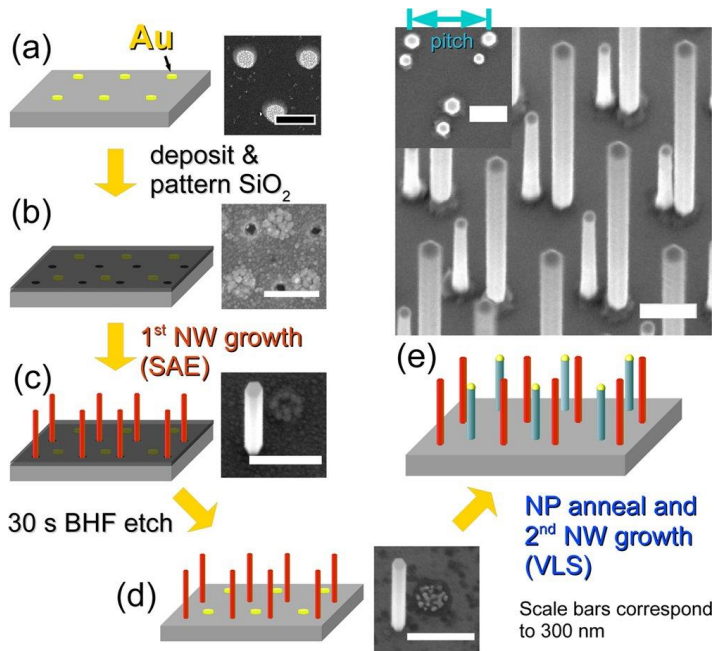


Figure 40. Process flow of the dual-type nanowire array fabrication. Two types of NWs are grown on a single GaAs substrate, the first NWs by SAE and second NWs with the VLS-method. The inset is showing a micrograph of the grown dual-type nanowires. [Publication VI]

Growing two types of nanowires on the same substrate affects the growth of the other. A parasitic growth is observed on the roots, sidewalls and on the top of the first grown NWs due to the increased surface area and the absence of the suppressing SiO₂ layer. The influence of the first set of grown NWs on the subsequently grown ones is shown in figure 41 which plots the average height of the first and second sets of NWs as well as that of reference NWs grown separately using only the second step. The same parameters are used for both dual-type VLS and the reference VLS-only growths. At a pitch array of 400 nm, the SAE grown NWs (blue) start to shadow the second grown VLS NWs. The height of secondly grown VLS NWs (red) decrease without reaching a saturation, whereas the SAE-grown NWs reach the saturation height at 650 nm pitch array. As can be seen, the shadowing effect shrinks the diameter of the second-grown NWs as shown in Figure 41b independent on the pitch.

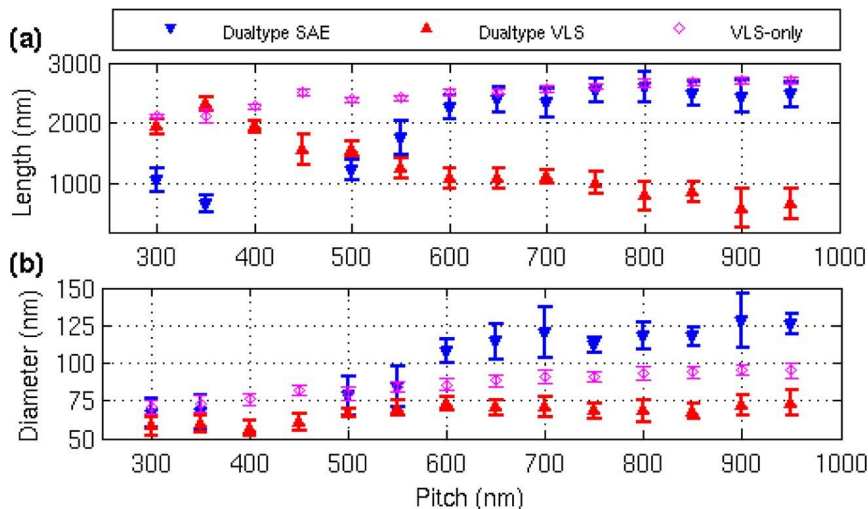


Figure 41. Average lengths and diameters of nanowires grown by dual-type and VLS methods. a) Average length of NWs as a function of pitch. b) Average diameter of NWs as a function of pitch. [Publication VI]

To demonstrate that the NWs can be grown with different chemistry with the described method is shown by growing another set of dual-type NWs, first SAE GaAs NW's from the TBA precursor followed by VLS InP NWs from the trimethylindium (TMIn) and tertiarybutylphosphine (TBP) precursors. The SAE grown GaAs NWs are shorter and VLS-grown InP NWs are the longer ones with the gold catalyst particle on top (Figure 42a). The orientation of VLS-grown NWs are random, due to colloidal gold being used for NP dispersion. Elemental analysis with EDX is used to confirm the results. The parasitic growth of In on the side walls of the first-grown GaAs NW is confirmed with an EDX measurements (Figure 42c).

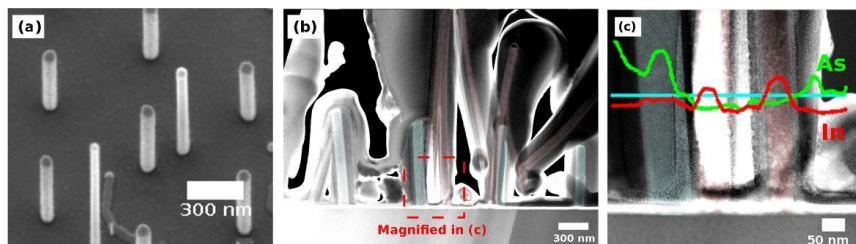


Figure 42. a) SEM-imaged tilted-angle view of GaAs (short ones) and InP (long ones) NWs. b) False color DF SEM micrograph of FIB cross-section of GaAs (blue) and InP (red) NWs. NWs are covered with a PECVD SiN and FIB Pt-deposited protective layers. c) Magnification of dashed area in (b) showing EDX measurement of the cross-section. The leftmost is GaAs NW, and two other are InP NWs. The EDX line scan is shown in cyan. [Publication VI]

Optical properties were compared from three 600 nm pitch array NW samples, dual-type GaAs/GaAs, VLS-grown GaAs- and SAE-grown GaAs samples. A lower reflectance was measured for the dual-type GaAs NWs compared to the single-type VLS and SAE control NWs (Figure 43a). The dual-type NWs exhibit enhanced light trapping which was an expected outcome as there is twice as many NWs per area ($\sim 6.4 \text{ NW}/\mu\text{m}^2$)

than the single-type arrays have ($\sim 3.2 \text{ NW}/\mu\text{m}^2$) on the same pitch. Light coupling into the NWs is known to depend on the NW diameter^{140,141}, but other physical parameters also play a role. As the substrate has two different types of nanowire arrays, the top layer that is composed solely from longer InP NWs has different refractive index (RI_1) than that of the other the lower layer (RI_2) having both short and long NWs (Figure 43b). The combined effect of the two different refractive indices present in the same array contributes to the reduction of the refractive index. The refractive index tuning of NWs have its merits in photovoltaic and photodetection applications.

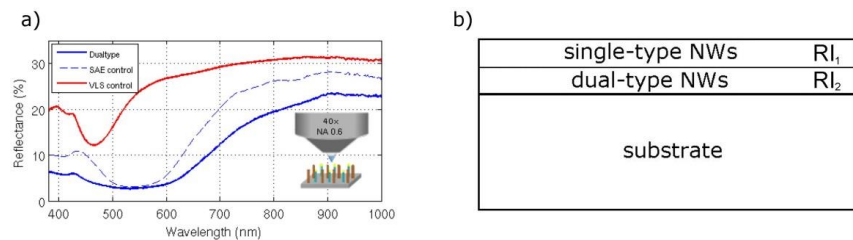


Figure 43. a) Refractive index measurement of three GaAs NW arrays. The measured RI for dual-type NWs is lower than either single-type NWs. [Publication VI] b) In the dual-type NWs the top layer consist solely of taller NWs, as the bottom layer has both NW types. The top layer is less dense than the bottom layer, and thus has a different RI than the bottom layer. The additional step in the refractive index is expected to cause the summed up RI to attenuate.

5. Summary And Outlook

Several charged-particle-beam characterization methods have been presented in this work, and complemented with fabrication of devices. The thesis introduced FIB-SEM techniques that were applied to imaging, elemental analysis, cross-sectional analysis, device fabrication and maskless nanofabrication. Due to being easy to operate, EM is a very popular imaging and characterization method in material science and biology. Electron tomography, especially the STEM method, is less commonly known or practiced, partially due to it being a more time-consuming and complex method. STEM tomography has a lot to offer in research. It is not uncommon that a new method is adopted by a small group of experts, before it diffuses to a wider user community. In the case of STEM tomography, the diffusion phase has been ongoing for several decades, which is surprisingly long time considering its impressive capabilities. The use of FIB as an analysis and fabrication tool is gaining more momentum as more systems are taken into use and new applications are being found. Since the conception of the idea of an LMIS, the FIB technique has been filling the gaps, where more conventional methods have failed, or have not worked so well.

The electron tomography method provides prominent alternatives for imaging small volume samples, with many advantages that conventional EM methods lack. A sample preparation and imaging method for Nafion is introduced, that enables STEM tomography at RT without causing any notable irradiation damage to a thin Nafion film. The shown method is capable of producing HR 3D reconstructions of beam-sensitive Nafion that has escaped other EM methods tried so far. Resolving the fine morphology of Nafion films provides a real-life example of a demanding challenge that many have tried to solve over the decades with a variety of methods with varying degrees of success. The STEM tomography results gained from Nafion thin films complement the previous results, and open up new pathways for further optimization of the material for specific applications. This could include the study presented in Publication II that was started with an incorporation of nanodiamonds into the Nafion film, that are shown to exhibit changes in ionic conduction properties. The Nafion composite film study could be taken further to investigate how the hydrophilic channel behavior is changed when channels are in direct contact with a diamond surface, and how this relates to the Nafion ionic filtering properties. The same can be said about the blood-test strip developed and discussed in Publication VIII. The ionic filtering properties of Nafion have been used to fabricate a disposable fin-

ger prick blood-test strip for quantitative point of care assay of acetaminophen in human blood plasma. The developed test strip that is cheap, fast and scalable for industrial mass production, could be further developed by improving its sensitivity, which heavily depends on the tailored morphology of the Nafion layer. The miniaturization of the active electrode area in the test strip is an obvious step forward that can be achieved by minor improvements in the fabrication process. Publication I is the first of its kind to study Nafion by staining the channels with UF. The UF behavior in the channels is far from conclusive, but this is one area that could be extended with careful planning and be backed up by comprehensive computer simulations.

FIB milling of an insulating SiN_x membrane is shown in Publication IV. FIB milling is used effectively in perforating a 100 nm thin silicon nitride membrane when realizing a thermally-isolated device platform. FIB milling charges the SiN_x membrane considerably, which is detrimental for the whole membrane if not taken care of. Charge-conductive milling patterns were tested and the best design was chosen for cancelling the charging originating from milling. The charge-cancelling patterns are fabricated on the membrane in the same process step as the devices on the platform. Conductive wirings act also as milling guidelines for the platform and suspending bridges. To separate the center part of the membrane from the silicon window edges, the intrinsic stress in the SiN_x membrane is reduced by releasing the membrane evenly from all four sides. When the adverse charging and stress in the membrane have been mitigated, the milling of the platform is finalized. The charge cancelling and brilliant milling strategy shown here proves the versatility of FIB.

The maskless silicon device fabrication discussed in Publication VII utilizes FIB gallium doping as a silicon etch stop-layer. Writing the desired pattern on top of a silicon surface with an ion beam is much faster than ion milling. The gallium-doped patterns are then exposed to a DRIE to define the final micro- or nano-device. The conventional hardmask deposition and associated lithography steps have been reduced to one FIB treatment, showing the flexibility of hybrid processing where the best sides of the two methods are combined. The parallel processing mode of the method is sufficient for small-batch production and acts as an extra alternative in nanoproto-typing. The possibilities for utilizing the method are unambiguously clear.

Corrosion protection of high-speed steel by ALD nanolaminates is presented in Publication III. The nanolaminates are deposited over the CrN corrosion protection layer that is grown by PVD on top of a steel substrate. ALD precursor gases are shown by FIB cross-sections to penetrate well into the cavities and pinholes of the PVD layer, forming a protective solid barrier layer for corrosion propagation. The results show that the corrosion of steel is reduced significantly. The effectiveness of the PVD/ALD composite layer is studied by repeated exposures of the surface to wear tests and saline solutions. The ALD coating initially increases the corrosion protection of the PVD CrN coating by two orders of magnitude, but is reduced by the increasing wear applied to the surface. The described method could be tested in similar applications where a hermetic sealing or corrosion protection of other substrates is required.

Additional future study could focus on finding more wear-resistant nanolaminates and coating materials.

Publication V describes how carbon nanowire fiber bundles are coated and saturated with electrodeposited copper. The copper increases the conductance of the pristine CNT bundles by nine fold and approaches the conductance of pure copper. The copper growth mechanism is revealed by analyses with SEM, EDX and FIB-SEM cross-sections.

Dual-type nanowires are grown on a single substrate in two growth steps. First SAE is applied for growing NWs in the first step, followed by VLS growth for the second type NWs. Different precursors can be chosen for the growth for tuning the chemistry of nanowires. Both the SAE- and VLS-grown NWs can be accurately positioned on the substrate in the EBL steps. The ability to control the diversity, position, dimensions and chemistry of the nanowires opens up possibilities for optimization of the optical properties of nanowires.

References

- [1] Gustafsson, M. G. L., Nonlinear structured-illumination microscopy: wide-field fluorescence imaging with theoretically unlimited resolution. *PNAS*, 102, 37, 13081-13086, 2005.
- [2] Hell, S. W., & Wichmann, J., Breaking the diffraction resolution limit by stimulated emission: stimulated-emission-depletion. *Opt. Lett.*, 19, 780-782, 1994.
- [3] Hosokawa, F., Sawada, H., Kondo, Y., Takayanagi, K., & Suenaga, K., Development of Cs and Cc correctors for transmission electron microscopy. *Microscopy*, 62, 1, 23-41, 2013.
- [4] Tanaka, N., Scanning transmission electron microscopy of nanomaterials, Chapter 2. Imperial College Press, London, 2015.
- [5] Wolf, S. G., Shimon, E., Elbaum, M. & Houben, L., STEM tomography in biology. *Cellular Imaging*, 33-60, 2017.
- [6] Ruska, H., Borries, B., & Ruska, E., Die bedeutung der übermikroskopie für die virusforschung. Springer, 1939.
- [7] Orloff, J. H., Study of a field-ionization source for microprobe applications. *J. Vac. Sci. Technol.*, 12, 6, 1209, 1975.
- [8] Krohn, V. E., & Ringo, G. R., Ion source of high brightness using liquid metal. *Appl. Phys. Lett.*, 27, 9, 479-481, 1975.
- [9] Postek, M T., & Vladar, A. E., Does your SEM really tell the truth? – How would you know? Part 4: Charging and its mitigation. *Scanning Microscopies*, 2015.
- [10] Bassim, N., & Notte, J., Focused ion beam instruments. Mater. Charact., ASM Handbook, 10, 635-670, 2019.
- [11] Hirsch, P., Kässer, M., Püttmann, M., & Reimer, L., Contamination in a scanning electron microscope and the influence of specimen cooling. *Scanning*, 16, 101-110, 1994.
- [12] Rose, A., Iams, H., Television pickup tubes using low-velocity electron-beam scanning. *Proc. I. R. E.*, 547-555, 1939.
- [13] Zworykin, V. K., Morton, G., & Malter, L., The secondary emission multiplier – a new electronic device. *Proc. Inst. Radio Eng.*, 24, 3, 351-375, 1936.
- [14] Rose, A. & Iams, H., The Orthicon, a television pick-up tube. *RCA Review*, Vol 4, 2, 186-199, 1939.
- [15] Touzin, M., Goeuriot, D., Guerret-Piécourt, C., Juvé, D., Tréheux, D., & Fitting, H-J., Electron beam charging of insulators: A self-consistent flight-drift model. *J. Appl. Phys.*, 99, 11, 114110, 2006.

- [16] Ohya, K., & Ishitani, T., Monte carlo study of secondary electron emission from SiO₂ induced by focused galium ion beams. *Appl. Surf. Sci.*, 237, 606-610, 2004.
- [17] Cazaux, J., Some considerations on the electric field induced in insulators by electron bombardment. *J. Appl. Phys.*, 59, 1418-1430, 1986.
- [18] Joy, D. C., & Joy, C., Dynamic charging in the low voltage SEM. *Microsc. Microanal.*, 1, 3, 109-112, 1995.
- [19] Joy, D. C., Joy, C. S., Low voltage scanning electron microscopy. *Micron.*, 27, 247-263, 1996.
- [20] Werner, H. W., & Morgan, A. E., Charging of insulators by ion bombardment and its mitigation for secondary ion mass spectrometry (SIMS) measurements. *J. Appl. Phys.*, 47, 1232-1242, 1976.
- [21] De Rosier, D. J., & A. Klug, Reconstruction of Three Dimensional Structures from Electron Micrographs. *Nature*, 217, 130-134, 1968.
- [22] Hart, R. G., Electron Microscopy of Unstained Biological Material: The Polytopic Montage. *Science*, 159, 1464-1467, 1968.
- [23] Hoppe, W., Langer, R., Knesch, G., & Poppe, C., Protein-Kristallstrukturanalyse mit Elektronenstrahlen. *Naturwissenschaften*, 55, 7, 333-336, 1968.
- [24] Holzer, L., & Cantoni, M., Review of FIB-tomography, Chapter 11. Nanofabrication Using Focused Ion and Electron Beams, Oxford University Press, New York, NY, USA, 2012.
- [25] Liu., Y, King, H. E., van Huis, M. A., Drury, M. R., & Plümper, O., Nanotomography of porous geological materials using focused ion beam-scanning electron microscopy. *Minerals*, 6, 104, 2016.
- [26] Xu, C. S., Hayworth, K. J., Lu, Z., Grob, P., Hassan, A. M., García-Cerdán, J. G., Krishna, K. N., Nogales, E., Weinberg, R. J. & Hess, H. F., Enhanced FIB-SEM systems for large-volume 3D imaging. *eLife*, 6, 1-36, 2017.
- [27] Frank, J., Electron Tomography: Three-dimensional Imaging with the Transmission Electron Microscopy. Plenum Press, New York, 1992.
- [28] Li, M-H., Yang, Y-Q., Huang, B., Luo, X., Zhang, W., Han, M., & Ru, J.-G., Development of advanced electron tomography in materials science based on TEM and STEM. *Trans. Nonferrous Met. Soc. China*, 24, 3031-3050, 2014.
- [29] Engelhardt, P., Electron tomography of chromosome Structure. *Encycl. Anal. Chem.*, John Wiley & Sons Ltd., 2006.
- [30] Koenig, J. L., Experimental IR spectroscopy of polymers – Chapter 3. Spectroscopy of Polymers, second ed., 77-145, 1999.
- [31] Volkert, C. A., & Minor, A. M., Focused ion beam microscopy and micromachining. *MRS Bulletin*, 32, 5, 389-399, 2007.
- [32] Prewett, P. D., & Mair, G. L. R., Focused Ion Beams from Liquid Metal Ion Sources. Research Studies Press, New York, Wiley, 1991.
- [33] Vogel, M., Handbook of Charged Particle Optics, 2nd ed. Contemporary Physics, Edited by J. Orloff, CRC Press, Boca Raton, 2009.
- [34] Gilbert, W., De Magnete, Book 2, Chapter 2, London, 1600. Translation by Motelay, P. F., Dover, New York, 1958.
- [35] Forbest, R. G., Understanding how the liquid-metal ion source works. *Vacuum*, 48, 1, 85-97, 1997.
- [36] Taylor, G. I., Disintegration of water drops in an electric field. *Proc. Roy. Soc. Lond.*, 280, 1382, 383-397, 1964.

- [37] Pillatsch, L., Östlund, F., & Michler, J., FIBSIMS: A review of secondary ion mass spectrometry for analytical dual beam focused ion beam instruments. *Prog. Cryst. Growth Charact. Mater.*, 65, 1, 1-19, 2018.
- [38] Bischoff, L., Mazarov, P., Bruchhaus, L., & Gierak, J., Liquid metal alloy ion sources – An alternative for focused ion beam technology, *Appl. Phys. Rev.* 3, 021101, 2016.
- [39] Marturi, N., Dembebel, S., & Piat, N., Depth and shape estimation from focus in scanning electron microscope for micromanipulation. 2013 International Conference on Control, Automation, Robotics and Embedded Systems (CARE), 2013.
- [40] Tseng, A. A., Recent developments in micromilling using focused ion beam technology. *J. Micromech. Microeng.*, 14, 4, R15-R34, 2004.
- [41] Shorubalko, I., Pillatsch, L., & Utke, I., Direct-write milling and deposition with noble gases. G. Hlawacek, A. Golzhauser (Eds.), Helium Ion Microscopy, Springer International Publishing, Chambridge, 355–393, 2016.
- [42] Ramezani, A. H., Sari, A. H., & Shokouhy, A., The effects of argon ion bombardment on the corrosion resistance of tantalum. *Int. Nano Lett.*, 7, 51-57, 2017.
- [43] Kim, S. W., Zheng, P., & Kato, K., Tilted ion implantation as a cost-efficient sub-lithographic patterning technique. *J. Vac. Sci. Technol. B*, 34, 4, 040608, 2016.
- [44] Delobbe, A., Salord, O., Hrnecir, T., David, A., Sudraud, P., & Lopour, F., High speed TEM sample preparation by Xe FIB. *Microsc. Microanal.*, 20, S3, 289-299, 2014.
- [45] Economou, N. P., Notte, J. A. & Thompson, W. B. The History and development of the helium ion microscope. *Scanning*, 34, 2, 83-89, 2011.
- [46] Ward, B. W., Notte, J. A., & Economou, N. P., Helium ion microscope: A new tool for nanoscale microscopy and metrology. *J. Vac. Sci. Technol. B Microelectron. Nanom. Struct.*, 24, 6, 2871, 2006.
- [47] Lemme, M. C., Bell, D. C., Williams, J. R, Stern, L. A., Baugher, B. W. H., Jarillo-Herrero, P., & Marcus, C. M., Etching of graphene devices with a helium ion beam. *ACS Nano*, 3, 2674, 2012.
- [48] Scipioni, L., Stern, L., & Notte, J., Applications of the helion ion microscope. *Microscopy Today*, 15, 6, 12-15, 2007.
- [49] Hill, R., Notte, J., & Ward, B., The ALIS He ion source and its application to high resolution microscopy. *Phys. Procedia*, 1, 1, 135-141, 2008.
- [50] Sijbrandij, S., Notte, J., Scipioni, L., Huynh, C., & Sanford, C., Analysis and metrology with a focused helium ion beam. *J. Vac. Sci. Technol. B Microelectron. Nanom. Struct.*, 28, 1, 73-77, 2010.
- [51] Chekurov, N., Grigoros, K., Peltonen, A., Franssila, S., & Tittonen, I., Localized gallium doping and cryogenic deep reactive ion etching in fabrication of silicon nanostructures. *Mater. Res. Soc. Symp. Proc.*, 1181, 2009.
- [52] Mayer, J., Giannuzzi, L. A., Kamino, T., & Michael, J., TEM sample preparation and FIB-induced damage, *MRS Bull.*, 32, 400-407, 2007.
- [53] Frey, L. Lehrer, C., & Ryssel, H., Nanoscale effects in focused ion beam processing. *Appl. Phys. A*, 76, 1017-1023, 2003.
- [54] Yogev, S., Levin, J., Molotskii, M., Schwarzman, A., Avayu, O., & Rosenwaks, Y., Charging of dielectrics under focused ion beam irradiation, *J. Appl. Phys.*, 103, 064107, 2008.

- [55] Chalapat, K., Chekurov, N., Li, J., & Paraoanu, G. S., Ion-beam assisted self-assembly of metallic nanostructures. *Nucl. Instrum. Methods Phys. Res. B*, 272, 202-205, 2012.
- [56] Lehrer, C., Frey, L., Petersen, S., & Ryssel, H., Limitations of focused ion beam nanomachining. *J. Vac. Sci. Technol., B*, 19, 6, 2533-2538, 2001.
- [57] Utke, I., Hoffmann, P., & Melngailis, J., Gas-assisted focused electron beam and ion beam processing and fabrication. *J. Vac. Sci. Technol. B*, 26, 1197-1276, 2008.
- [58] Mulders, J. J. L., & Botman, A., Towards electron beam induced deposition improvements for nanotechnology. Functional Nanoscience, Bozen, Italy, 179-192, 2011.
- [59] Gazzadi, G. C., Frabboni, S., Menozzi, C., & Incerti, L., Electrical characterization of suspended Pt nanowires grown by EBID with water vapour assistance. *Microelectron. Eng.*, 85, 1166-1169, 2008.
- [60] Harriott, L. R. *et al.*, Integrated Circuit Repair Using Focused Ion Beam Milling. *J. Vac. Sci. Technol., B*, 4, 1, 181-184, 1986.
- [61] Shaver, D. C., Integrated Circuit Diagnosis Using Focused Ion Beams. *J. Vac. Sci. Technol., B*, 4, 1, 185-188, 1986.
- [62] Melngailis, J., Focused Ion Beam Technology and Applications. *J. Vac. Sci. Technol., B*, 5, 2, 469-495, 1987.
- [63] Casey, J. D., Doyle, A. F., Lee, R. G., & Stewart D. K., Gas-assisted etching with focused ion beam technology. *Microelectron. Eng.*, 24, 43-50, 1994.
- [64] Ray, V., Fluorocarbon precursor for high aspect ratio via milling in focused ion beam modification of integrated circuits. Proceedings from the 30th International Symposium for Testing and Failure Analysis, 534-537, 2004.
- [65] Rubanov, S., & Munroe, P. R., FIB-Induced damage in silicon. *J. Microsc.*, 214, 3, 213-221, 2004.
- [66] Loeber, T. H., Laegel, B., Wolff, S., Schuff, S., Balle, F., Beck, T., Eifler, D., Fitschen, J. h., & Steidl, G., Reducing curtaining effects in FIB/SEM applications by a goniometer stage and an image processing method. *J. Vac. Sci. Technol., B*, 35, 6, 2017.
- [67] Zhu, X., Zhang, Y., Zhang, J., Xu, J., Ma, Y., Li, Z., & Yu, D. Ultrafine and smooth full metal nanostructures for plasmonics. *Adv. Mater.*, 22, 39, 4345-4349, 2010.
- [68] Cui, Z., Micro-Nanofabrication: Technologies and applications. Springer, 77-138, 2005.
- [69] Pengcheng, L., A Review of proximity effect correction in electron-beam lithography. arXiv:1509.05169v1, 2015.
- [70] Xia, Y., Rogers, J. A., Paul, K. E., & Whitesides, G. M., Unconventional methods for fabricating and patterning nanostructures. *Chem. Rev.*, 99, 7, 1823-1848, 1999.
- [71] Auffan, M., Santaella, C., Thiéry, A., Paillés, C., Rose, J., Achouak, W., Thill, A., Masion, A., Wiesner, M., & Bottero, Y. -J., Electron beam lithography (EBL). *Encycl. Nanotechnol.*, 718-740, 2012.
- [72] Watakabe, Y., Kato, T., Shigetomi, A., & Morimoto, H., Mask fabrication for VLSI using an electron beam exposure system. *J. Vac. Sci. Technol.*, 21(4), 1005-1011, 1982.

- [73] Plummer, J. D., Deal, M. D., Griffin, P. G., Silicon VLSI technology – fundamentals, practice and modelling. Prentice Hall, Inc. Upper Saddle River, New Jersey, ISBN 0-13-085037-3, 2000.
- [74] Carlsson, J.-O., & Martin, P. M., Chemical vapor deposition. Handbook of Deposition Technologies for Films and Coatings, Elsevier Inc., 314-363, 2010.
- [75] Ohring, M., Chemical vapor deposition. Materials Science of Thin Films, 277-355, 2002.
- [76] Zvonkov, B. N., Vikhrova, O. V., Danilov, Y. A., Demina, P. B., Dorokhin, M. V., & Podol'skii, V. V., Using laser sputtering to obtain semiconductor nanoheterostructures. *J. Opt. Technol.*, 75, 6, 389-393, 2008.
- [77] Facsko, S., Formation of ordered nanoscale semiconductor dots by ion sputtering. *Science*, 285, 5433, 1551-1553, 1999.
- [78] Rubio, F., Denis, J., Albella, J. M., & Martinez-Duart, J. M., Sputtered Ta₂O₅ antireflection coatings for silicon solar cells. *Thin Solid Films*, 90, 405-408, 1982.
- [79] Lugscheider, E., Barimani, C., Wolff, C., Guerreiro, S., & Doepper, G., Comparison of the structure of PVD-thin films deposited with different deposition energies. *Surf. Coat. Technol.*, 86-87, 177-183, 1996.
- [80] Campbell, S. A., The Science and engineering of microelectronic fabrication. Oxford University Press, 295-321, 2001.
- [81] Baptista, A., Silva, F., Porteiro, J., Míguez, J., & Pinto, G., Sputtering physical vapour deposition (PVD) coatings: A critical review on process improvement and market trend demands. *Coatings*, 8, 11, 402, 2018.
- [82] Glocker, D. A., & Shah, S. I., Handbook of thin film process technology. Institute of Physics Publishing, Bristol, 1995.
- [83] Deringer, V. I., Caro, M. A., Jana, R., Aarva, A., Elliot, S. R., Laurila, T., Csányi, G., & Pastewka, L., Computational surface chemistry of tetrahedral amorphous carbon by combining machine learning and density functional theory. *Chem. Mater.*, 30, 7438-7445, 2018.
- [84] Puurunen, R. L., Surface chemistry of atomic layer deposition: A case study for the trimethylaluminum/water process. *J. Appl. Phys.*, Applied Physics Reviews, 97, 2005.
- [85] George, S. M., Atomic layer deposition: An overview. *Chem. Rev.*, 110, 111-131, 2010.
- [86] Feng, X., Peng, H., Gong, J., Wang, W., Liu, H., Quan, Z., Pan, S., & Wang, L., Epitaxial growth of InN thin films by plasma-enhanced atomic layer deposition. *J. Appl. Phys.*, 124, 243104, 2018.
- [87] Kukushkin, S. A., Osipov, A. V., & Romanychev, A. I., Epitaxial growth of zinc oxide by the method of atomic layer deposition on SiC/Si substrates. *Phys. Solid State*, 58, 1448-1452, 2016.
- [88] O'Brien, N. J., Rouf, P., Samii, R., Rönby, K., Buttera, S. C., Hsu, C.-W., Ivanov, I. G., Kessler, V., Ojamäe, L., & Pedersen, H., In situ activation of an indium(III) triazenide precursor for epitaxial growth of indium nitride by atomic layer deposition. *Chem. Mater.*, 32, 11, 4481-4489, 2020.
- [89] Stringfellow, G. B., Fundamental aspects of MOVPE. Metalorganic Vapor Phase Epitaxy (MOVPE): Growth, Materials Properties, and Applications, John Wiley & Sons Ltd., 19-69, 2020.

- [90] Garcia, I., Galiana, B., Rey-Stolle, I., & Algora, C., MOVPE technology for the growth of III-V semiconductor structures. 2007 Spanish Conference on Electron Devices, 2007.
- [91] Anooz, S. B., Grüneberg, R., Chou, T-S., Fiedler, A., Irmscher, K., Wouters, C., Schewski, R., Albrecht, M., Galazka, Z., & Miller., W., Impact of chamber pressure and Si-doping on the surface morphology and electrical properties of homoepitaxial (100) β -Ga₂O₃ thin films grown by MOVPE. *J. Phys. D: Appl. Phys.*, 54, 034003, 2020.
- [92] Samuelson, L., Self-forming nanoscale devices. *Mater. today*, 6, 10, 22-31, 2003.
- [93] Wang, H., Zepeda-Ruiz, L. A., Gilmer, G. H., & Upmanyu, M., Atomistics of vapour-liquid-solid nanowire growth. *Nat. Commun.*, 4, 1, 2013.
- [94] Li, S., et al., Vapour-liquid-solid growth of monolayer MoS₂ nanoribbons. *Nat. Mater.*, 17, 6, 535-542, 2018.
- [95] Wagner, R. S., Whisker technology. Levitt, A. P. (ed.), Wiley, New York, 1970.
- [96] Johansson, J., Overgaard, N. C., & Magnusson, M. H., The compositional homogeneity of the metal particle during vapor-liquid-solid growth of nanowires. *Sci. Rep.*, 10, 1, 11041, 2020.
- [97] Wagner, R. S., & Ellis, W. C., Vapor-liquid-solid mechanism of single crystal growth. *Appl. Phys. Lett.*, 4, 89-90, 1964.
- [98] Yazawa, M., Koguchi, M., & Hiruma, K., Heteroepitaxial ultrafine wirelike growth of InAs on GaAs substrates. *Appl. Phys. Lett.*, 58, 1080, 1991.
- [99] Haraguchi, K., Katsuyama, T., Hiruma, K., & Ogawa, K., GaAs pn junction formed in quantum wire crystals. *Appl. Phys. Lett.*, 60, 745, 1992.
- [100] Kukovitsky, E. F., L'vov, S. G., & Sainov, N. A., VLS-growth of carbon nanotubes from the vapor. *Chem. Phys. Lett.*, 317, 65-70, 2000.
- [101] Choi, H. J., Vapor-liquid-solid growth of semiconductor nanowires. In Yi, G. C. (eds) *Semiconductor Nanostructures for Optoelectronic Devices*. NanoScience and Technology, Springer, Berlin, Heidelberg, 1-36, 2012.
- [102] Rothman, A., Dubrovskii, V. G., & Joselevich, E., Kinetics and mechanism of planar nanowire growth. *PNAS*, 117, 1, 152-160, 2019.
- [103] Pauzauskie, P. J., & Yang, P., Nanowire photonics. *Mater. Today*, 9, 10, 36-45, 2006.
- [104] Laermer, F., Process for etching structures in an etching body using a plasma comprising modulating the intensity of the plasma as a function of time, US-Pat. Appl., 2004/0173571.
- [105] Rahan, N., Zorman, C. A., Mehregany, M., Deanna, R., & Harvey, R. J., Effect of MEMS-compatible thin film hard coatings on the erosion resistance of silicon micromachined atomizers. *Surf. Coat. Technol.*, 108-109, 391, 1998.
- [106] Pattekar, A. V., & Kothare, M. K., A Radial microfluidic fuel processor. *J. Power Sources*, 147, 116, 2005.
- [107] Glière, A., & Delattre, C., Modeling and fabrication of capillary stop valves for planar microfluidic systems. *Sens. Actuators A*, 130-131, 601, 2006.
- [108] Gorowitz, B., & Saia, R. J., Reactive ion etching. VLSI electronics microstructure science, 297-339, 1984.
- [109] Elwenspoek, M., & Jansen, H., Silicon micromachining. Cambridge University Press, 1998.

- [110] Arnold, J. C., & Sawin, H. H., Charging of pattern features during plasma etching. *J. Appl. Phys.*, 70, 5314, 1991.
- [111] Walter, L., Photoresist damage in reactive ion etching. *J. Electrochem. Soc.*, 144, 2150-2154, 1997.
- [112] Baldi, A., Lei, M., Gu, Y., Stiegel, R. a., Ziaie, B., A Microstructured silicon membrane with entrapped hydrogels for environmentally sensitive fluid gating. *Sens. Actuators B*, 114, 9, 2006.
- [113] Walker, M. J., Comparison of Bosch and cryogenic processes for patterning high aspect features in silicon. *Proc. SPIE* 4407, 89-99, 2001.
- [114] de Boer, M. J., Tjerkstra, R. W., Berenschot, J. W., Janesen, H. V., Burger, G. J., Gardeniers, J. G. E., Elwenspoek, M., & Van den Berg, A., Micromachining of buried micro channels in silicon. *J. Microelectromech. Syst.*, 9, 1, 94-103, 2000.
- [115] Langford, R. M., Nellen, P. M., Gierak, J., & Fu. Y., Focused ion beam micro- and nanoengineering. *MRS Bulletin*, 32, 5, 417-423, 2007.
- [116] Leivo, M. M., & Pekola, J. P., Thermal characteristics of silicon nitride membranes at sub-Kelvin temperatures. *Appl. Phys. Lett.*, 72, 11, 1305-1307, 1998.
- [117] Leivo, M., & Pekola, J. P., Thermal characteristics of silicon nitride membranes at sub-Kelvin temperatures. *Appl. Phys. Lett.*, 72, 11, 1305-1307, 1998.
- [118] Serra, E., Bawaj, M., Borrielli, A., Di Giuseppe, G., Forte, S., Kralj, N., et al., Microfabrication of large-area circular high-stress silicon nitride membranes for optomechanical applications. *AIP Advances*, 6, 065004, 2016.
- [119] Rollier, A.-S., Legrand, B., Deresmes, D., Lagouge, M., Collard, D., & Buchaillot, L., Tensile stress determination in silicon nitride membrane by AFM characterization. The 13th International Conference on Solid-State Sensors, Actuators and Microsystems, 2005.
- [120] Shu, B., Zhang, H., Xuan, R., Dai, X., Hu, H., Song, J., Liang, L., & Cui, L., Fabrication of high compressive stress silicon nitride membrane in strained silicon technology. 2009 IEEE International Conference of Electron Devices and Solid-State Circuits (EDSSC), 365-367, 2009.
- [121] Sievilä, P., Chekurov, N., & Tittonen, I., The fabrication of silicon nanostructures by focused-ion-beam implantation and TMAH wet etching. *Nanotechnology*, 21, 145301, 2010.
- [122] Chekurov, N., Grigoros, K., Peltonen, A., Franssila, S. & Tittonen, I., The fabrication of silicon nanostructures by local gallium implantation and cryogenic deep reactive ion etching. *Nanotechnology*, 20, 2009.
- [123] Kusoglu, A., Weber, A. Z., New insights into perfluorinated sulfonic-acid ionomers. *Chem. Rev.*, 117, 987-1104, 2017.
- [124] Chen, W., Cui, F., Liu, L., & Li, Y., Assembled Structures of Perfluorosulfonic acid ionomers investigated by anisotropic modelling and simulations. *J. Phys. Chem. B*, 121, 41, 9718-9724, 2017.
- [125] Schmidt-Rohr, K., & Chen, Q., Parallel cylindrical water nano-channels in Nafion fuel-cell membranes. *Nat. Mater.*, 7, 75-83, 2008.
- [126] Moussy, F., & Harrison, D. J., Prevention of the rapid degradation of subcutaneously implanted Ag/AgCl reference electrodes using polymer coatings. *Anal. Chem.*, 66, 5, 674-679, 1994.
- [127] Mauritz, K. A., & Moore, R. B., State of understanding Nafion. *Chem. Rev.*, 104, 10, 4535-4586, 2004.

- [128] Sainio, S., Nordlund, D., Caro, M. A., Gandhiraman, R., Koehne, J., Wester, N., Koskinen, J., Meyyappan, M., & Laurila, T., Correlation between sp³-to-sp² ratio and surface oxygen functionalities in tetrahedral amorphous carbon (ta-C) thin film electrodes and implications of their electrochemical properties. *J. Phys. Chem.*, 120, 8298-8304, 2016.
- [129] Palomäki, T., Wester, N., Caro, M. A., Sainio, S., Protopopova, V., Koskinen, J., & Laurila, T., Electron transport determines the electrochemical properties of tetrahedral amorphous carbon (ta-C) thin films. *Electrochim. Acta*, 225, 1-10, 2015.
- [130] Allen, F. I., Comolli, L. R., Kusoglu, A., Modestino, M. A., Minor, A. M. & Weber, A. Z., Morphology of hydrated as-cast Nafion revealed through cryo electron tomography. *ACS Macro Lett.*, 4, 1-5, 2015.
- [131] Pfab, J., & Si, D., Automated threshold selection for cryo-EM density map, 2019.
- [132] Wester, N., Mynttinen, E., Etula, J., Lilius, T., Kalso, E., Kauppinen, E. I., Laurila, T., & Koskinen, J., Simultaneous detection of morphine and codeine in the presence of ascorbic acid and uric acid and in human plasma at Nafion single-walled carbon nanotube thin-film electrode. *J. ACS Omega*, 4, 17726–17734, 2019.
- [133] Wester, N., Mynttinen, E., Etula, J., Lilius, T., Kalso, E., Mikladal, B. F., Zhang, Q., Jiang, H., Sainio, S., Nordlund, D., et al., Single-walled carbon nanotube network electrodes for the detection of fentanyl citrate. *ACS Appl. Nano Mater.*, 3, 1203–1212, 2020.
- [134] Wisniewski, N., & Reichert, M., Methods for reducing biosensor membrane biofouling. *Colloids Surf., B: Biointerfaces*, 18, 197-219, 2000.
- [135] Härkönen, E., Kolev, I., Díaz, B., Swiatowska, J., Maurice, V., Seyeux, A., Marcus, P., Fenker, M., Toth, L., Radnoczi, G., Vehkamäki, M., & Ritala, M., Sealing of hard CrN and DLC coatings with atomic layer deposition. *ACS Appl. Mater. Interfaces*, 6, 3, 1893-1901, 2014.
- [136] Leppäniemi, J., Sippola, P., Broas, M., Aromaa, J., Lipsanen, H., & Koskinen, J., Corrosion protection of steel with multilayer coatings: Improving the sealing properties of physical vapor deposition CrN coatings with Al₂O₃/TiO₂ atomic layer deposition nanolaminates. *Thin solid films*, 627, 59-68, 2017.
- [137] Puurunen, R. L., & Gao, F., Influence of ALD Temperature on Thin Film Conformality: Investigation with Microscopic Lateral High-Aspect-Ratio Structures. 14th International Baltic Conference on Atomic Layer Deposition (BALD), IEEE, 20–24, 2016.
- [138] Subramaniam, C., Yamada, T., Kobashi, K., Sekiguchi, A., Futaba, D. N., Yumura, M., et al., One hundred fold increase in current carrying capacity in a carbon nanotube-copper composite. *Nat. Commun.*, 4, 2013.
- [139] Grujicic, D., & Pesic, B., Electrodeposition of copper: the nucleation mechanisms. *Electrochim. Acta*, 47, 18, 2901-2912, 2002.
- [140] Wu, P. M., Anttu, N., Xu, H. Q., Samuelson, L., Pistol, M.-E., Colorful InAs nanowire arrays: From strong to weak absorption with geometrical tuning. *Nano Lett.*, 12, 1990–1995, 2012.
- [141] Seo, K., Wober, M., Steinvurzel, P., Schonbrun, E., Dan, Y., Ellenbogen, T., & Crozier, K. B., Multicolored vertical silicon nanowires. *Nano Lett.*, 11, 1851–1856, 2011.



ISBN 978-952-64-0510-0 (printed)

ISBN 978-952-64-0511-7 (pdf)

ISSN 1799-4934 (printed)

ISSN 1799-4942 (pdf)

Aalto University
School of Electrical Engineering
Department of Micro- and Nanosciences
www.aalto.fi

**BUSINESS +
ECONOMY**

**ART +
DESIGN +
ARCHITECTURE**

**SCIENCE +
TECHNOLOGY**

CROSSOVER

**DOCTORAL
DISSERTATIONS**